Two-Coordinate Coinage Metal Complexes as Solar Photosensitizers

Collin N. Muniz,† Claire A. Archer,† Jack S. Applebaum, Anushan Alagaratnam, Jonas Schaab, Peter I. Djurovich, Mark E. Thompson*

Department of Chemistry, University of Southern California, Los Angeles, CA 90089, United States of America

Abstract

Generating a sustainable fuel from sunlight plays an important role in meeting the energy demands of the modern age. Herein we report two-coordinate carbene-metal-amide (cMa, M = Cu(I) and Au(I)) complexes can be used as sensitizers to promote the light driven reduction of water to hydrogen. The cMa complexes studied here absorb visible photons ($\varepsilon_{vis} > 10^3$ $M^{-1}cm^{-1}$), maintain long excited state lifetimes ($\tau \sim 0.2$-1 μs) and perform stable photo-induced charge transfer to a target substrate with high photoreducing potential ($E^{+/}$* up to -2.33 V vs. $Fc^{+/0}$ based on a Rehm-Weller analysis). We pair these coinage metal complexes with a cobalt-glyoxime electrocatalyst to photocatalytically generate hydrogen and compare the performance of the copper- and gold-based cMa complexes. We also find that these two-coordinate complexes presented can perform photo-driven hydrogen production from water without the addition of the cobalt-glyoxime electrocatalyst. In this "catalyst free" system the cMa sensitizer partially decomposes to give metal nanoparticles that catalyze water reduction. This work identifies two-coordinate coinage metal complexes as promising abundant metal, solar fuels photosensitizers that offer exceptional tunability and photoredox properties.

Introduction

Generating fuels *via* solar photocatalysis is a highly active research field in chemistry today.[1] Molecular light-driven chemistry requires two primary processes: light absorption and chemical interaction with a substrate to store the light energy in the form of a fuel. These tasks are often divided between two different molecules. Light absorption occurs at the photosensitizer (PS), which transfers charge onto an electrocatalyst that performs the chemical transformation. Complexes such as $Ru(bpy)_3^{2+}$ and $Ir(ppy)_3$ are commonly used photosensitizers owing to their high molar absorptivity ($\varepsilon \sim 10^4$ $M^{-1}cm^{-1}$), long-lived excited states, and their high stability in

oxidized and reduced forms.[2] These properties enable the complexes to efficiently deliver charge to a variety of electrocatalysts from their excited state. The main drawback of Ru/Ir compounds is that they are among the rarest metals on earth, which precludes their use in scalable and sustainable energy technology.[3]

Chemists have responded to the challenge of developing sustainable solutions by exploring metal complexes of earth abundant metals as viable alternatives. Significant efforts have been put into first row transition metals, among which copper has been a rising candidate to match the performance of scarce metals.[4] The few reported classes of copper(I) photosensitizers use complexes with a four-coordinate structure. Prominent classes pioneered by the McMillin group are cationic Cu(I)(N^N)$_2$ or Cu(I)(N^N)(P^P) complexes (where N^N is a bis-imine ligand, such as a phenanthroline or bipyridine derivative, and P^P = is a bis-phosphine derivative).[5] These complexes display visible absorption assigned to metal-to-ligand charge-transfer (MLCT) transitions that have molar absorptivities greater than 10^3 $M^{-1}cm^{-1}$ and lifetimes for emission that vary from 10^2 to 10^5 ns. Compounds such as Cu(dmp)$_2^+$ (dmp = 2,9-dimethyl-1,10-phenanthroline) and Cu(dap)(Xantphos) (dap = 2,9-bis(4-methoxyphenyl)-1,10-phenanthroline, Xantphos = (9,9-dimethyl-9H-xanthene-4,5-diyl)bis(diphenylphosphane)) have been successfully employed in photoredox catalysis.[4c, 5b, 6] However, an inherent restriction in the photophysical properties in these Cu(I) derivatives is Jahn-Teller distortion of the MLCT state in fluid solution.[7] The accompanying rapid non-radiative decay will often lead to short lifetimes of the excited state, thereby diminishing the effectiveness of the compounds as photosensitizers. Significant efforts from the McMillin and Castellano groups have shown that installing bulky functional groups at the 2,9-position of phenanthroline and methylating in the 3,4,7,8-positions significantly inhibits Jahn-Teller distortion, extending the excited state lifetime to the microsecond regime.[8]

Two-coordinate coinage metal complexes with carbene-metal-amide (cMa) structure have recently been studied for applications in organic LEDs but have not been investigated for photoredox catalysis.[9] These two-coordinated compounds have several attributes that are advantageous to their application as photosensitizers. The lowest energy absorption band of cMa complexes is typically an interligand charge transfer (ICT) transition with a hole localized on the carbazole and an electron on the carbene. Thus, the absorption energy is easily tuned throughout the visible spectrum by the choice of either carbene or amide, which is of considerable benefit in

comparison to the four-coordinate complexes where the energy of the MLCT state is primarily adjusted by varying the energy of the ligand-localized LUMO.[9a, 9d, 9e, 10] The redox potentials of the cMa complexes can also be varied over a wide range by judicious selection of the carbene and substituents on the amide. Finally, the ICT state is not susceptible to Jahn-Teller distortion, thus leading to low rates for non-radiative decay and high photoluminescence efficiency. However, it is valid to question whether these two-coordinate complexes have sufficient stability to serve as effective photosensitizers. The ligands are monodentate making them kinetically labile. The molecules are also coordinatively unsaturated, which could allow for deleterious non-radiative decay of the excited state via solvent coordination. Solvent coordination and exciplex formation is a well-documented issue in Cu(I) complexes that results in a decrease of excited state lifetime even for the sterically protected four-coordinate complexes.[11]

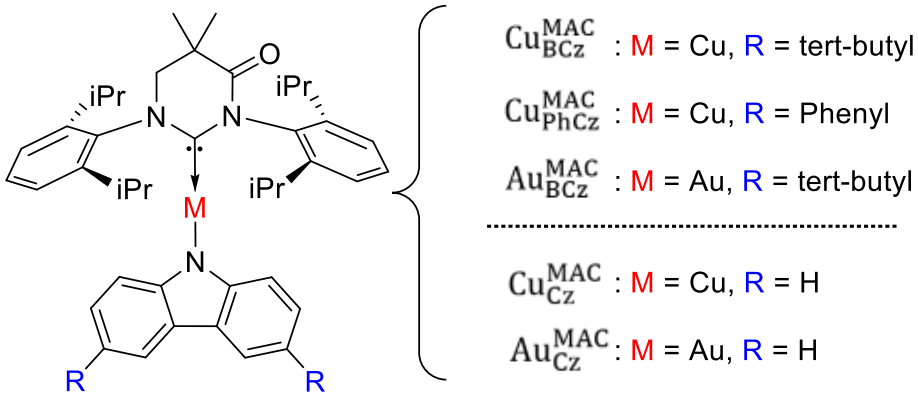

Figure 1. Structure of the three photosensitizers investigated in this work: M^{MAC}_{RCz}[M = Cu or Au, R = tert-butyl (B) or phenyl (Ph)] (iPr = isopropyl). M^{MAC}_{Cz} were reported previously and were used for comparison in this study.[9e]

In this work, we probe the excited state photoredox capabilities of several two-coordinate cMa complexes in a variety of solvents to evaluate the suitability of these compounds as a new class of Cu(I) and Au(I) photosensitizers. The carbene and carbazole ligands for the complexes were chosen here to ensure visible light absorption with long excited state lifetimes (Figure 1). While all of the complexes are stable to electrochemical reduction, it is well known that carbazole is unstable to oxidation as it oligomerizes at the 3,6-positions.[12] Thus, alkyl or aryl substituents at the 3,6-sites were installed to increase the stability of the oxidized cMa complex. Oxidation potentials for the excited states ($E^{+/*}$) were estimated from electrochemical and steady state photophysical measurements and confirmed using a Rehm-Weller analysis for each

photosensitizer. The role of the metal was investigated by comparing properties of Cu(I) and Au(I) derivatives with a common amide (3,6-di-tert-butylcarbazole), and that of the amide was probed by varying the substituent groups in Cu_{RCz}^{MAC} (R = tert-butyl or phenyl). We find that two-coordinate cMa complexes are a viable new class of photosensitizers for solar photochemistry, demonstrating the photo-driven production of hydrogen from water, both with and without an added cobalt-glyoxime electrocatalyst.

3. Experimental

Synthesis: All reactions were performed under a N_2 atmosphere using a Schlenk line. Tetrahydrofuran (THF), dichloromethane, and toluene were dried over alumina using a solvent purification system by SG Water USA, LLC. Dimethylformamide (DMF) and acetonitrile (MeCN) were purchased as dry solvents from VWR. Precursor complexes 1,3-bis(2,6-diisopropylphenyl)-5,5-dimethyl-4-oxo-3,4,5,6-tetrahydropyrimidin-1-ium-2-ide M(I) chloride (M_{Cl}^{MAC} [M = Cu(I) or Au(I)]) were prepared according to literature precedent.[9e] The amide precursors 3,6-di-tert-butyl-9H-carbazole and 3,6-di-phenyl-9H-carbazole were purchased from AK Scientific and Tokyo Chemical Industry, respectively. Sodium tert-butoxide was purchased from Sigma Aldrich. Reference compounds Cu_{Cz}^{MAC} and Au_{Cz}^{MAC} were prepared according to literature procedures.[9e] All purchased chemicals were used without further purification.

The general synthesis of all reported compounds involved adding solid carbazole (or substituted carbazoles) and NaO^{t}Bu to a freshly dried Schlenk-flask connected to a Schlenk line and a nitrogen atmosphere was established. THF was injected against positive N_2 pressure, and the mixture stirred at room temperature for one hour to generate free carbazolide. The M_{Cl}^{MAC} (M = Cu or Au) complex was next added against positive N_2 pressure. The flask was then covered with aluminum foil and allowed to stir at room temperature overnight. All subsequent workup was performed in air. The workup involved filtering the reaction solution through Celite and removing the solvent with a rotary evaporator (rotovap). The crude solid was dissolved in 50/50 MeCN/hexane by volume, and product was extracted into the MeCN phase. The MeCN solution was evaporated on the rotovap to yield a sticky yellow gel. The gel was redissolved in 20/80 CH_2Cl_2/hexane by volume and the solvent removed on the rotovap, which converted the gel-like solid to a powder. The process of dissolving in 20/80 CH_2Cl_2/hexane and solvent removal was repeated three times to yield a fine yellow powder. Lastly, the solid was washed copiously with

either methanol or diethyl ether to yield analytically pure samples. The detailed synthesis and analytical data for each cMa sensitizer is given in the Supporting Information (SI).

Computation: Density functional theory (DFT) and time dependent DFT (TDDFT) calculations were performed in QChem v5.0 to predict the structural and electronic properties of the cMa photosensitizers in the ground and excited states. Geometry optimizations were performed using the B3LYP method, LACVP basis, and Fit-LACVP effective core potential (ECP).[13] TDDFT calculations were performed using the LACVP basis, fit-LACVP ECP, and the CAM-B3LYP exchange (attenuation parameter = 0.2) with RPA enabled. Orbital composition analysis and wavefunction overlap of the HOMO and LUMO were evaluated using Multiwfn.[14]

Electrochemistry: Cyclic voltammetry (CV) and differential pulse voltammetry (DPV) measurements were performed with a VeraSTAT potentiostat using a glassy carbon working electrode, platinum counter electrode, and silver wire as a pseudo-reference electrode. Solutions were prepared in dry, N_2 sparged solvents with 0.1M tetrabutylammonium hexafluorophosphate electrolyte concentration. CV and DPV measurements were performed with scan rates of 0.1 Vs^{-1}, and 10 mVs^{-1}, respectively. Measurements were repeated using ferrocene or decamethylferrocene as an internal standard; all potentials were referenced to the ferrocenium/ferrocene ($Fc^{+/0}$) couple.

Photophysical Measurements: Absorption spectra were recorded using a Hewlett-Packard 4853 diode array spectrometer. Photoluminescence (PL) spectra were recorded using a Photon Technology International QuantaMaster spectrofluorimeter. Excited state lifetime measurements were performed using time correlated single photon counting (TCSPC) with an IBH Fluorocube apparatus interfaced to a Horiba FluoroHub+ controller. Quantum yield (QY) measurements were performed using a Hamamatsu C9920 integrating sphere with a xenon lamp excitation source. Samples for PL, TCSPC, and QY measurements were prepared in a custom made long, glass cuvette that allowed the solutions to be sparged with N_2 and sealed with a Teflon valve. More information on the cuvette design is available in figure S3.

Stern-Volmer Quenching: Quenching of the excited state via photo-induced electron transfer from PS^* to Q was measured by TCSPC. Deactivation of the excited state via energy transfer was avoided by choosing quenchers that had energies for their T_1 state higher than that of the PS. Five solutions were prepared with a constant photosensitizer concentration (~10 μM) and increasing quencher concentration. The optical spectra were measured to ensure that the absorption

features of the PS did not change, showing little or no interaction of PS and Q is present in the ground state (no static quenching). Oxygen-free conditions were established by sparging solutions with N_2 to prevent quenching of PS^* by oxygen. Excited state lifetimes (τ) were measured as a function of increasing quenching concentration ([Q]) and compared to the lifetime without quencher (τ_0). The Stern-Volmer equation was used to extract the rate constant k_q corresponding to quenching of the excited state.

$$\frac{\tau_0}{\tau} = 1 + k_q \tau_0 [Q] \quad (1)$$

Plots of τ_0/τ vs. [Q] yield a linear line with R^2 values near unity. For a given Stern-Volmer plot, the slope was divided by τ_0 to yield values for k_q.

Photocatalysis: The cobalt-glyoxime electrocatalyst [$Co(dmgH)_2pyCl$] was synthesized according to literature procedure.[15] The sacrificial reductant 1,3-dimethyl-2-phenyl-2,3-dihydro-1H-benzo[d]imidazole (BIH) was purchased from AmBeed .[16] Solutions were prepared in a N_2-filled glovebox. A 50 mL Schlenk flask was charged with either Au_{BCz}^{MAC} or Cu_{PhCz}^{MAC}, $Co(dmgH)_2pyCl$, and 224 mg BIH. All solids were dissolved in 5 mL of THF/water (5% water by volume). The flask was capped with a rubber septum. The flask was placed in front of a 470 nm LED (model number M470L5) with focusing optics (model number SM1U25-A & SM1RC) purchased from Thorlabs (Figure S18). The flask was wrapped in foil apart from a small area for the focused blue light to enter the reaction flask. The flask was placed ~6 inches from the LED with an incident power of 486 mW and the reaction was stirred with a magnetic stir bar.

Photocatalytic hydrogen production was quantified using a Thermo Finnigan Trace GC 2000 with a thermal conductivity detector and nitrogen as a carrier gas. The GC internal temperature was 70 °C at the time of sample injection. The temperature was maintained for 7 minutes followed by an increase to 100 °C at a rate of 15 °C/min. The final temperature of 100 °C was maintained for two minutes. A calibration curve was created by injecting different volumes of 5% H_2 in N_2 gas using a Hamilton gastight 500 μL syringe and integrating the area of the hydrogen peak in the chromatogram. A linear relationship with $R^2 > 0.99$ was established in the integrated area vs. volume of hydrogen injected as seen in Figure S19. Samples were illuminated for a set amount of time to generate hydrogen. The LED was then turned off and gas was drawn from the photoreaction headspace through the rubber septum and injected into the GC. The integral

of the hydrogen peak in the chromatogram was used to determine the volume of hydrogen in the syringe based on the calibration curve. This quantity was related to the volume of hydrogen produced in the reaction, which allowed us to calculate turn over numbers (TONs) with respect to the electrocatalyst (moles H_2/moles $Co(dmgH)_2pyCl$) and/or sensitizer (moles H_2/moles M^{MAC}_{amide}).

4. Results and Discussion

Synthesis. The cMa compounds were synthesized using methods that follow literature precedent.[9e] The copper complexes were isolated with >63% yield, and Au^{MAC}_{BCz} was isolated with 31% yield. The final products are all indefinitely air stable as solids. The composition was characterized by ^1H and ^{13}C NMR, CHNS elemental analysis (See SI for more details).

Molecular structures of Cu^{MAC}_{BCz}, Au^{MAC}_{BCz} and Cu^{MAC}_{PhCz} were determined using single crystal X-ray diffraction. Structural drawings of the three complexes are given in Figure S1. The Au^{MAC}_{BCz} complex crystallized with a disorder of the C=O and the two methyl groups whereas Cu^{MAC}_{BCz} and Cu^{MAC}_{PhCz} do not show any disorder in the MAC ligands in their structures. Values for the bond lengths and angles were similar to parameters found in related cMa derivatives.[9a-e] The three cMa complexes have linear coordination geometries as the C-M-N bond angles are all near ~180°. The carbene and carbazole ligands have near coplanar orientations, with the torsion angles between that vary between 6.2° to 19.6° (Table S1). It has been shown that coplanar ligand orientation is important for achieving appreciable oscillator strength of the ICT transition.[9f, 9g, 17] Derivatives of cMa complexes with ligands having large torsion angles display ICT bands with notably low oscillator strengths because the π systems of the ligands have poor spatial overlap.[9f, 18]

Computational Results. The electronic structure of the complexes in the ground state was examined using DFT calculations for the cMa complexes. All materials have their highest occupied molecular orbital (HOMO) localized on the carbazole, and lowest unoccupied molecular orbital (LUMO) localized on the carbene. Both orbitals show only a small contribution from the metal d orbital involved with π-bonding to the coordinating atom of each ligand.

The energies for the HOMO in the cMa complexes are altered by substituents on the carbazole ligand, whereas the energies for the LUMO remain effectively constant because the complexes have the same carbene ligand (Table 1). The energy of the HOMO for the Cu analogues is destabilized in the order $Cu^{MAC}_{BCz} > Cu^{MAC}_{Cz} > Cu^{MAC}_{PhCz}$, which is consistent with the electron

donating nature of the ^{t}Bu group and electron withdrawing nature of the phenyl group. Changing the metal from copper to gold also stabilizes the HOMO, which is ascribed to the higher ionization potential of Au(I) relative to Cu(I).[19] The choice of metal ion does not affect the LUMO energies due to the nature of the dative carbene-metal bond compared to the relatively ionic M^+- Cz^- interaction.

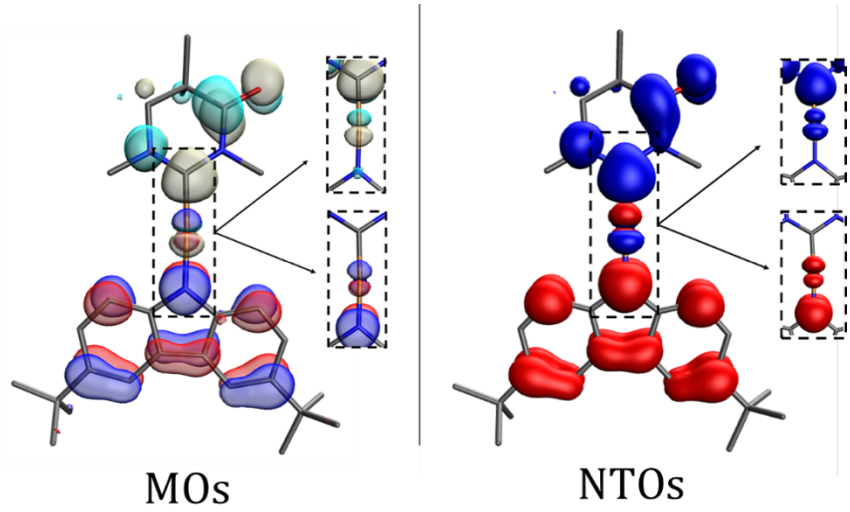

Figure 2. The HOMO [red/blue] and LUMO [cyan/beige] wavefunctions (left), and hole [red] and electron [blue] NTO wavefunctions (right) of Cu_{BCz}^{MAC} displayed with isovalue = 0.1. Hydrogen atoms and the 3,6-diisopropylphenyl groups were omitted for clarity. The HOMO/LUMO densities of Cu_{PhCz}^{MAC} and Au_{BCz}^{MAC} are qualitatively the same (see Figure S2).

Table 1. Computational results of each photosensitizer. Here, *f* corresponds to the oscillator strength of the transition, and $\Lambda_{h+,e-}$ is the overlap between the hole and electron wavefunctions.

	HOMO (eV)	LUMO (eV)	$S_0 \rightarrow S_1$ (eV/*f*)	$S_0 \rightarrow T_1$ (eV)	ΔE_{ST}[a] (eV)	% metal (HO/LU)	$\Lambda_{h+,e-}$ (S_1) (%)
Cu_{BCz}^{MAC}	-4.08	-1.99	2.41/0.12	2.19	0.22	4.4/7.8	27
Cu_{Cz}^{MAC}	-4.17	-1.99	2.48/0.11	2.26	0.22	4.6/7.8	26
Cu_{PhCz}^{MAC}	-4.23	-2.08	2.51/0.14	2.32	0.19	3.3/7.8	25
Au_{BCz}^{MAC}	-4.22	-1.98	2.59/0.19	2.33	0.26	4.1/9.0	31
Au_{Cz}^{MAC}	-4.32	-1.99	2.66/0.16	2.41	0.25	4.3/9.1	36

Analysis of the excited states using TDDFT shows that the hole and electron wavefunctions in the $S_0 \rightarrow S_1$ transition are well described by the HOMO and LUMO, respectively (Figure 2) .

Localization of the HOMO and LUMO on the donor and acceptor ligands characterizes the interligand charge transfer excited state. The energy of the ICT state mirrors the trend in HOMO energy since the energy of the LUMO is largely invariant in these complexes. The energy of the T_1 state lies close to the S_1 state because of the large spatial separation between the hole and electron centers of charge for two-coordinate cMa complexes. The small exchange energies, along with strong spin-orbit coupling imparted by the metal, are known to promote rapid $T_1 \rightarrow S_1$ intersystem crossing and thermally assisted delayed fluorescence (TADF) in two-coordinate complexes with coplanar ligands.[9b, 20] Comparing Cu_{BCz}^{MAC} and Cu_{Cz}^{MAC} to their gold analogues shows an increase in oscillator strength for the ICT transition for the gold analogs. This property is consistent with the trend in HOMO/LUMO overlap ($\Lambda_{h+,e-}$), which suggests the Au(I) metal center provides greater orbital overlap than Cu(I). This difference in overlap is interesting because the metal d orbital contributes a small, albeit important, point of overlap between the HOMO and LUMO. To further investigate this feature, the contribution of the metal atom in each orbital was computed using the Hirshfeld method.[14] The product of the metal orbital contribution to the HOMO and LUMO ($\%M_{HOMO} \times \%M_{LUMO}$) is greater for the gold complexes (36-39%) with respect to their copper analogs (26-36%). This difference leads to an increase in oscillator strength for the ICT transition in the Au derivative.

Photophysical Properties. The photophysical properties of the cMa complexes were examined in polar and non-polar solvents. All compounds display broad, featureless absorption bands in the visible spectrum which are assigned to an ICT transition (Figure 3). These bands have values for molar absorptivity (ε = 4000-8000 $M^{-1}cm^{-1}$) consistent with charge transfer transitions.[21] The energy of the ICT band blue-shifts in the order $Cu_{BCz}^{MAC} < Cu_{PhCz}^{MAC} < Au_{BCz}^{MAC}$. This hypsochromic shift is due to the stabilization of the HOMO in Cu_{PhCz}^{MAC} and Au_{BCz}^{MAC}, as discussed above. The Cu_{PhCz}^{MAC} complex has a higher molar absorptivity than Cu_{BCz}^{MAC} stemming from π-extension by the aryl substituents of 3,6-diphenylcarbazole. The molar absorptivity for Au_{BCz}^{MAC} is greater than that of Cu_{BCz}^{MAC} owing to the increase in NTO overlap induced by the more diffuse 5d orbitals of gold relative to 3d orbitals on copper (Table 1).

Luminescence spectra for the cMa complexes are broad and featureless, with a large Stokes shift, and are assigned to TADF emission from an ICT state (Figure 3b). The quantum yields (Φ) are 0.17 and 0.15 for Cu_{BCz}^{MAC} and Au_{BCz}^{MAC} with excited state lifetimes (τ) of 350 ns and 250 ns in

THF, respectively. The decrease in lifetime for the gold complex is due to the simultaneous increase in the radiative and non-radiative rates (k_r and k_{nr}, see Table 2). Replacing the tert-butyl substituents with phenyl groups in Cu^{MAC}_{PhCz} results in a decrease of k_{nr} which increases both the photoluminescence efficiency ($\Phi = 0.43$) and lifetime ($\tau = 460$ ns).

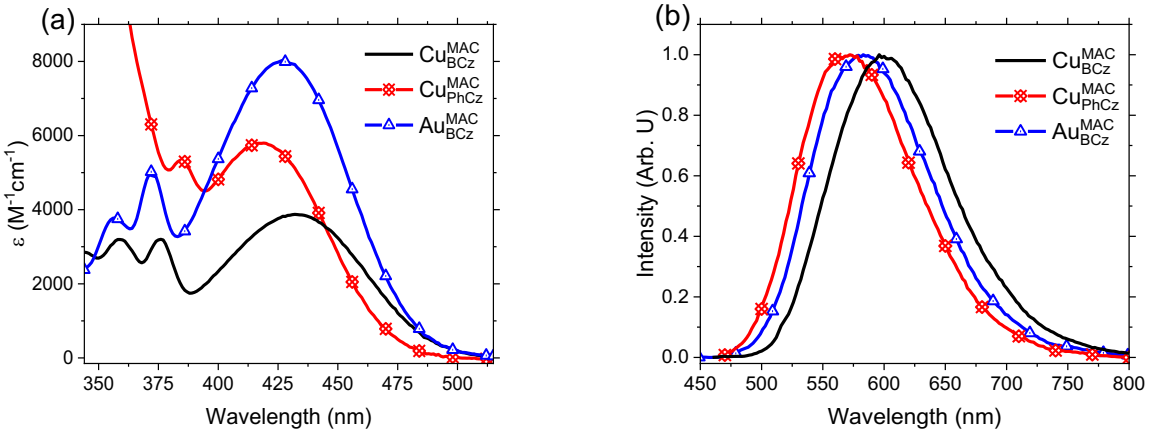

Figure 3. (a) Molar absorptivity and (b) the emission of all compounds in THF. The full spectrum from 250 nm to 550 nm is provided in Figure S4.

Photophysical properties vary in solvents of varying polarity (toluene, THF, CH_2Cl_2, MeCN, and DMF). The solvent dependent absorption and emission spectra are shown in Figures S5-S6. The absorption band for the ICT transition blue shift with increasing solvent polarity, whereas the emission spectra red shift. This solvatochromism has been previously explained by the large change in dipole between the ground and excited state of these molecules.[9c] Here we observe that solvatochromism is markedly more pronounced in the absorption spectrum than the emission spectrum.

An important consideration for a photosensitizer is the lifetime of the excited state, which must persist long enough for the PS^* to diffuse to an electrocatalyst and transfer charge. The diffusion limited rate constant of electron transfer (k_q) plateaus at ~$1x10^{10}$ $M^{-1}s^{-1}$ for highly endergonic electron transfer processes.[22] The total intermolecular electron transfer rate depends directly on the concentration of the quenching agent ([Q]), *i.e.* the electrocatalyst. Quencher concentrations of 1-10 mM will lead to quenching rates ($k_q = 1x10^7$ s^{-1} to $1x10^8$ s^{-1}) that correspond to lifetimes for the quenched PS (τ = 100-10 ns) that define lower limits for the useful effective lifetime of the photosensitizer.

Table 2. Photophysical parameters for toluene, THF, and MeCN solutions.

	solvent	λ_{max} abs (nm)	λ_{max} em (nm)	τ (ns)	Φ	k_r ($10^5 s^{-1}$)	k_{nr} ($10^5 s^{-1}$)
Cu^{MAC}_{BCz}	toluene	455	574	720	0.34	4.7	9.2
	THF	435	603	350	0.17	4.7	24
	MeCN	403	607	120	0.04	3.4	81
Cu^{MAC}_{PhCz}	toluene	445	556	710	0.70	9.9	4.2
	THF	424	578	460	0.43	9.4	12
	MeCN	393*	584	190	0.16	8.4	44
Au^{MAC}_{BCz}	toluene	449	568	450	0.36	8.0	14
	THF	427	584	250	0.15	6.0	34
	MeCN	400	600	69	0.04	5.8	140

* Values cannot be accurately determined because the ICT absorption band overlaps with the ligand localized transitions at higher energy.

The excited state lifetimes and quantum yields also vary as a function of solvent polarity (see Table 2 for toluene, THF and MeCN and Table S4 for CH_2Cl_2 and DMF). The luminescence lifetimes for all photosensitizers decrease with increasing solvent polarity owing to increases in non-radiative decay (See Figure S8). Complexes in toluene solution have the longest excited state lifetimes and the most intense absorption of visible light. The enhanced absorption of visible light due to the red shift of the ICT transition with decreasing solvent polarity. However, non-polar solvents can lead to additional kinetic barriers for ion separation after intermolecular charge transfer. Of note is the fact that the copper complexes have the longest emission lifetimes in any given solvent. This property can be advantageous in improving the photocatalytic efficiency by making electron transfer quenching of the excited state (k_q) a more competitive deactivation pathway than the non-productive processes (k_r and k_{nr}).

Electrochemical properties. Electrochemical measurements were performed to evaluate the ground state redox potentials and reversibility of the cationic and anionic species of the cMa complexes in a variety of solvents that are suitable for solar fuels production, *i.e.* THF, DMF and MeCN.[23] The redox potentials measured in CH_2Cl_2 and THF are given in Table 3; potentials recorded in DMF and MeCN are given in Table S5. The electrochemical reversibility is strongly

influenced by the identity of the solvent, whereas the redox potentials are near solvent independent. Reduction is reversible for all cMa complexes across all solvents and the potential remains effectively constant. This behavior is consistent with the LUMO being localized on the MAC carbene ligand common to all the complexes. The trend in oxidation potentials also follows the trends computed for the energy of the HOMO. The value of $E^{+/0}$ for Cu_{Cz}^{MAC} is greater than that of Cu_{BCz}^{MAC} and Cu_{PhCz}^{MAC} but less than that of the Au analog.

Table 3. Electrochemical potentials of cMa complexes in various solvents. Potentials are in Volts vs. $Fc^{+/0}$ couple. The full CV and DPV for all complexes in CH_2Cl_2, THF, DMF, and MeCN can be found in the SI (Figures S9 – S12).

	CH_2Cl_2			THF	
	$E^{+/0}$	$E^{0/-}$		$E^{+/0}$	$E^{0/-}$
Cu_{BCz}^{MAC}	0.06 *rev*	*	Cu_{BCz}^{MAC}	0.06 *rev*	-2.54 *rev*
Cu_{PhCz}^{MAC}	0.17 *rev*	*	Cu_{PhCz}^{MAC}	0.12 *rev*	-2.62 *rev*
Au_{BCz}^{MAC}	0.13 *rev*	*	Au_{BCz}^{MAC}	0.18 *rev*	-2.62 *rev*
Cu_{Cz}^{MAC}	0.19 *irr*	*	Cu_{Cz}^{MAC}	0.18 *irr*	-2.61 *rev*
Au_{Cz}^{MAC}	0.22 *irr*	*	Au_{Cz}^{MAC}	0.28 *irr*	-2.55 *rev*

* Reductions are outside of the solvent window. *rev* = reversible, *irr* = irreversible

The cMa complexes with unsubstituted carbazolyl ligands (Cu_{Cz}^{MAC} and Au_{Cz}^{MAC}) undergo irreversible oxidation in CH_2Cl_2 and THF as shown in Figure 4. Oxidation is also irreversible in DMF and MeCN (Figures S9 andS10). This response is to be expected since the HOMO localized on carbazolyl ligand irreversibly oxidizes due to a radical coupling reaction after proton loss at the 3,6-positions.[12] Weak cathodic waves at ~ -0.25 V to 0.2 V for these cMa complexes that appear after the second cycle are thus assigned to oxidation of the oligomerization products as the features are absent in derivatives substituted on the 3,6-position. Hence, tert-butyl or phenyl groups at these sites leads to enhanced oxidative stability in CH_2Cl_2 and THF on the timescale of seconds. However, the cMa complexes are all irreversibly oxidized in MeCN (Figure S10). In contrast, Au_{BCz}^{MAC} maintains a notable return wave in DMF, whereas a weak return oxidation wave is found for the Cu(I) derivative. These results suggests that decomposition occurs by nucleophilic attack at the metal-amide linkage in MeCN, and that this bond is stronger for Au-amides than for the Cu

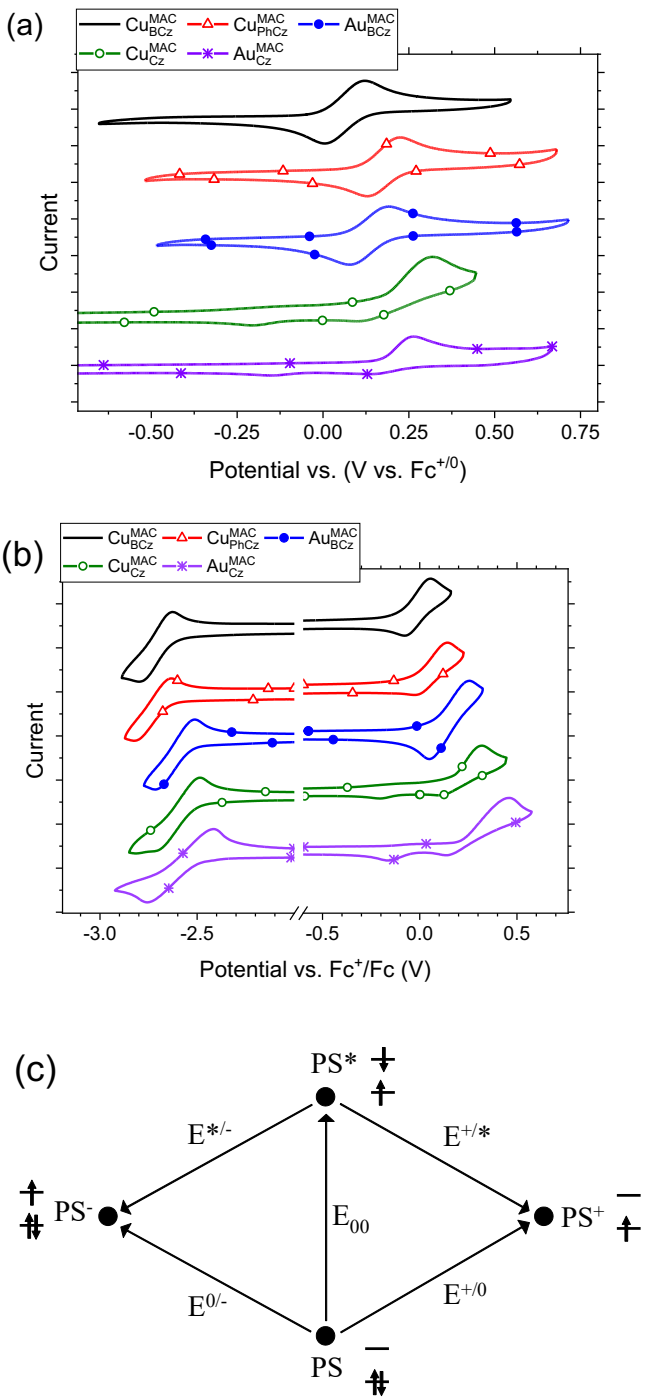

Figure 4. Cyclic voltammetry of all complexes in CH_2Cl_2 (a) and THF (b). The reduction event was outside of the solvent window for CH_2Cl_2 therefore, only the oxidative sweeps are shown here. (c) Latimer diagram relating the ground state photosensitizer (PS) to the excited state (PS*) through ground state and excited state redox couples, and the optical excited state energy (E_{00}).

analogs. Based on these experiments, we chose to perform quenching studies in THF because it sustains reversible oxidation and reduction for all photosensitizers. Furthermore, THF gives the strongest absorptivity for cMa complexes among polar solvents, while also being sufficiently polar to facilitate efficient charge separation after electron transfer reactions.

Redox Properties of the Excited State. Molecules in the excited state are more potent oxidizing and reducing agents than in their ground state. Redox potentials in the excited state are related to the redox potentials in the ground state and the energy gained by absorbing a photon. These potentials are approximated using Equations 2 and 3.[24]

$$E^{+/*} = E^{+/0} - E_{00} \quad (2)$$

$$E^{*/-} = E^{0/-} + E_{00} \quad (3)$$

where E_{00} is the energy corresponding to the midpoint between the $S_0 \rightarrow S_1$ absorption and $S_1 \rightarrow S_0$ emission. This relationship is shown graphically in Figure 4c.

Table 4. Ground and excited state redox potentials for the cMa complexes in THF.[a]

	$E^{+/0}$ (V)	$E^{0/-}$ (eV)	E_{00} (eV)	$E^{+/*}$ (V)	$E^{*/-}$ (V)
Cu_{BCz}^{MAC}	0.01	-2.65	2.44	-2.43	-0.21
Cu_{PhCz}^{MAC}	0.12	-2.65	2.57	-2.45	-0.08
Au_{BCz}^{MAC}	0.13	-2.60	2.51	-2.38	-0.09

[a] Potentials are referenced to internal $Fc^{+/0}$.

Using Equations 2 and 3, the cMa complexes are predicted to be potent photo-reducing agents, with near equal values of $E^{+/*}$ (-2.4 V vs. $Fc^{+/0}$), whereas being only mild photo-oxidants. The near degeneracy of $E^{+/*}$ reflects the trend in increasing energy of E_{00} (Cu_{BCz}^{MAC} > Cu_{PhCz}^{MAC} > Au_{BCz}^{MAC}) being offset by an increase in oxidation potential for each complex. This behavior is to be expected in a system where the energy of the S_1 state is dictated by a transition involving the energy of a spatially separated HOMO and LUMO. Substituents that stabilize/destabilize the oxidation potential will correspondingly raise/lower the E_{00} energy. Thus, the value for $E^{+/*}$ is largely governed by the choice of carbene. Analogously, the value for $E^{*/-}$ is approximately governed by the choice of metal and amide donor since these moieties determine the energy of the HOMO. Photo-oxidative quenching of the cMa complexes was therefore investigated due to their remarkably high $E^{+/*}$ values.

The thermodynamic driving force of quenching an excited state via electron transfer (ΔG) depends on the values of $E^{+/*}$ of the photosensitizer $\left(E_{PS}^{+/*}\right)$, $E^{0/-}$ of the quencher $\left(E_{Q}^{0/-}\right)$, and work terms (W_s) associated with coulombic interactions of separating charged species in the solvent medium (Eq 4).[25]

$$\Delta G = \left(E_{PS}^{+/*} - E_{Q}^{0/-}\right) + W_s \quad (4)$$

As the quenching molecule becomes harder to reduce, the rate of electron transfer is expected to decrease sharply when $\Delta G > 0$. The initial step for electron transfer from the excited photosensitizer (PS^*) to a quenching molecule (Q) requires the two species to diffuse together to form an encounter complex [PS*,Q] with rate constant k_d (Scheme 1). This encounter complex can relax through concomitant radiative and non-radiative processes (k_r and k_{nr}), or it can be quenched

by transferring an electron or energy to the quencher. Here, we focus only on quenching via charge transfer by choosing quenchers that have energies for their S_1 and T_1 states well above those of the cMa complexes, precluding quenching by energy transfer. Electron transfer occurs with a rate constant k_{eT}, and the resultant charge separated pair [PS^+,Q^-] can either recombine by back electron transfer with rate constant k_{beT}, or return to the ground state with rate constant k_{re}. The charge separated pair can also diffuse away from each other as individual species ($PS^+ + Q^-$) with rate constant k_s.

Scheme 1. Kinetic scheme for the oxidative quenching of a photosensitizer.

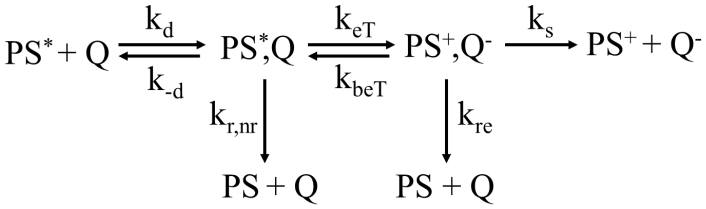

Rehm and Weller showed that the net quenching rate constant k_q given by Eq 5 must consider the equilibrium which forms the encounter complex ($k_d/k_{-d} = \Delta V_{1,2}$), and charge recombination (k_{re}):

$$k_q = \frac{k_d}{1 + \left(\frac{k_d}{\Delta V_{12} \times k_{re}}\right)\left(\exp\left(\frac{\Delta G^{\ddagger}}{RT}\right) + \exp\left(\frac{\Delta G}{RT}\right)\right)} \tag{5}$$

where R is the ideal gas constant, T is temperature, and ΔG is given by Eq 3.[26] The free energy term ($\Delta G^{\ddagger}$) accounts for the reorganization energy of (PS^*,Q) to (PS^+,Q^-) and the solvent reorganization required for electron transfer (ΔG_r).

$$\Delta G^{\ddagger} = \left[\left(\frac{\Delta G}{2}\right)^2 + (\Delta G_r)^2\right]^{\frac{1}{2}} + \frac{\Delta G}{2} \tag{6}$$

Rate constants of luminescence quenching for each complex were derived from Stern-Volmer analysis of experiments performed in THF using quenchers with varying reduction potentials; quinoxaline (QNX), N-methylpthalimide (NMeP), N,N-dimethyl-4-nitroaniline

(DMNA), nitrobenzene (NB), and perinapthenone (PN). The reduction potentials for each quencher is given in Table 5 and plots of Stern-Volmer quenching data are given in the SI (Figures S15 - S17).

Table 5. Stern-Volmer quenching rate constants (k_q) for the cMa complexes measured in THF. Reduction potentials of the quenching molecules were measured using differential pulse voltammetry (Figure S13) and are reported vs. $Fc^{+/0}$.

	$E^{0/-}$ (V)	$k_q(Cu_{BCz}^{MAC})$ (10^9 $M^{-1}s^{-1}$)	$k_q(Cu_{PhCz}^{MAC})$ (10^9 $M^{-1}s^{-1}$)	$k_q(Au_{BCz}^{MAC})$ (10^9 $M^{-1}s^{-1}$)
QNX	-2.18	0.064	0.14	--
NMeP	-1.92	2.3	3.1	0.8
DMNA	-1.90	2.8	3.5	2.1
NB	-1.62	9.9	11	8.0
PN	-1.50	11	11	9.5

Analysis of the Stern-Volmer data for a given quenching molecule shows that rate of k_q is fastest for Cu_{PhCz}^{MAC} and slowest for Au_{BCz}^{MAC} (Table 5). This behavior mirrors the energy of $E^{+/}$* for the complexes estimated using Eq 2. An increase in k_q is also apparent as $E^{0/-}$ for the quencher becomes less negative. This change is due to an increase in the driving force of electron transfer from PS^* to Q ($\Delta G^{\ddagger}$) with increasing electron affinity of the quencher. When the driving force becomes significantly large, k_q plateaus at $1.1x10^{10}$ s^{-1}, which corresponds to diffusion-limited quenching. In this regime, the slowest step in Scheme 1 is diffusion of PS^* to Q to form the encounter complex (PS^*,Q). Thus, the value for k_d in the Rehm-Weller fit was set to $1.1x10^{10}$ s^{-1}. Details for the other parameters used in the fits are given in the SI. Values of $E^{+/}$* for each complex were determined from fits of the quenching rates to Eq 5 (Figure 5). Values for $E^{+/}$* can be obtained from fits to the data in Figure 5 (-2.28 V for Cu_{BCz}^{MAC}, -2.33 V for Cu_{PhCz}^{MAC}, and -2.23 V for Cu_{BCz}^{MAC}). Thus, the trend in k_q parallels the same trend in oxidation potential of the complexes (Cu_{PhCz}^{MAC} > Cu_{BCz}^{MAC} > Au_{BCz}^{MAC}). This analysis suggests that the small difference in $E^{+/}$* values found for the three complexes is consistent with the predictions of Eq 2, yet 100-170 meV lower than the estimates of -2.4 V. The disparity can be accounted for by considering that E_{00} used in Eq 2 is

based on the $S_0 \rightarrow S_1$ transition. Intersystem crossing is extremely rapid in the cMa complexes ($k_{ISC} > 10^9$ s^{-1}) and they are likely quenched out of the long-lived triplet excited state (T_1).[9e] The energy of the T_1 state for Au_{Cz}^{MAC} was reported to be 90 meV lower than the S_1 state, which accounts for most of the difference in $E^{+/*}$.[9a] Similar ΔE_{ST} values are expected for the other derivatives because experimental values for ΔE_{ST} in cMa complexes do not vary significantly between Cu and Au congeners, and substituents to the amide ligand do not contribute significantly to the hole NTO.

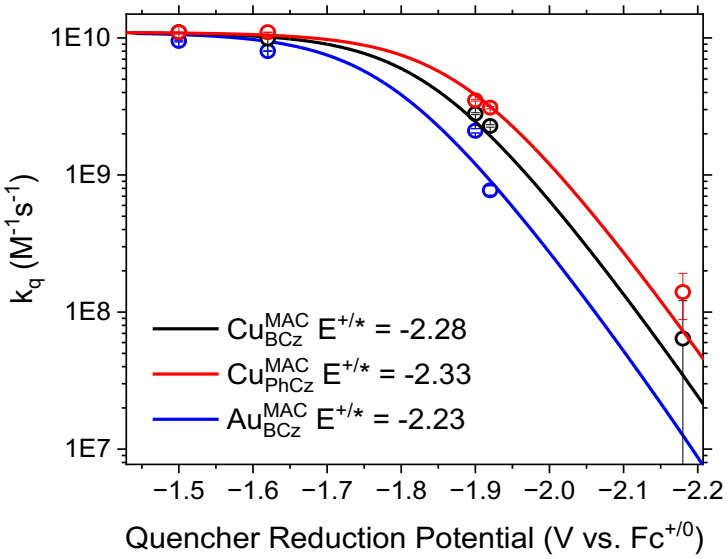

Figure 5. Rehm-Weller analysis of the cMa complexes in THF.

Several quenching studies were also performed in toluene, but values of k_q for a given photosensitizer-quencher pair were consistently lower when compared to values found in THF (See Figure S16 and Table S6). This effect is likely due to the non-polar nature of toluene which increases the work term (W_s in Eq 4) and consequently the energy barrier (ΔG_r in Eq 6) for charge separation. Non-polar media also inhibits physical separation of the charged species in the cage complex (PS^+,Q^-), which can allow the rate of k_{bet} to become competitive with k_{et}. This effect is expected to lower the overall efficiency of charge transfer, and thus k_q. Alternatively, several quenching studies were performed in MeCN (Table S7). Quenching rates for a given photosensitizer-quencher pair are faster in highly polar MeCN than in THF since the work term becomes negligible in MeCN, which yields a larger driving force in ΔG and a concomitant increase in k_q. However, the benefit from the faster quenching rate is offset by the hypsochromic shift for

the ICT transition in MeCN, which decreases the amount light absorbed within the visible portion of the solar spectrum.

Photoproduction of H_2. To demonstrate the viability of cMa complexes as solar photosensitizers, hydrogen evolution reactions (HER) were carried out the using a well-established electrocatalyst for water reduction, $Co(dmgH)_2pyCl$. We chose this compound because it uses an earth abundant metal, is readily synthesized and has been extensively studied for HER.[23c, 27] Two reduction events at -1.0 V and -1.7 V vs. $Fc^{+/0}$ in $Co(dmgH)_2pyCl$ have been ascribed to $Co^{III/II}$ and $Co^{II/I}$ couples which generate the active species for water reduction (Figure S14).[28] Therefore, our Rehm-Weller analysis predicts that all three cMa complexes can photoreduce $Co(dmgH)_2pyCl$ with a driving force ≥ 500 meV. The Au_{BCz}^{MAC} and Cu_{PhCz}^{MAC} complexes were chosen as they have near equal values for $E^{*/-}$ (Table 4), which makes for direct comparisons of gold to copper. A Stern-Volmer study using Au_{BCz}^{MAC} confirmed that the excited cMa complex was effectively quenched by $Co(dmgH)_2pyCl$ (k_q = 2.5x10^9 $M^{-1}s^{-1}$, Figure S20). The measured k_q is near the diffusion limit which is consistent with data in Figure 5. BIH was chosen as the sacrificial reductant as it has an oxidation potential ($E^{+/0}$ = -0.07 V vs. Fc/Fc^+)[29] sufficient to reduce Cu_{PhCz}^{MAC} and Au_{BCz}^{MAC} in the excited state ($E^{*/-}$ ~ -0.08 V and -0.09 V, respectively). BIH was recently found to efficiently reduce photo-excited Au_{BCz}^{MAC}* to $(Au_{BCz}^{MAC})^-$ (k_q = 2.5x10^8 $M^{-1}s^{-1}$),[30] albeit at a rate ten-fold slower than $Co(dmgH)_2pyCl$. Thus, there are two thermodynamically viable pathways to photocatalytically reduce $Co(dmgH)_2pyCl$ using an excited cMa photosensitizer (Figure 6). In route 1, $Co(dmgH)_2pyCl$ (CAT) oxidizes the cMa* complex to the cMa^+ cation, which is subsequently reduced by BIH (SAC). Alternatively, in route 2, BIH reduces cMa* to cMa^-, and the anion is subsequently oxidized by $Co(dmgH)_2pyCl$. Therefore, the dominant catalytic pathway to reduce the HER catalyst depends on the relative concentrations of $Co(dmgH)_2pyCl$ and BIH in the reaction mixture. Route 1 is favored when [$Co(dmgH)_2pyCl$] > [BIH], whereas route 2 is favored when [BIH] >> [$Co(dmgH)_2pyCl$].

The photophysical properties of the photosensitizer and HER catalyst dictate which reaction pathway is preferred during the HER process. For example, a near saturated solution of $Co(dmgH)_2pyCl$ (16 mM, $k_q[Q] = 4x10^7$ s^{-1}) is needed to effectively quench the photo-excited cMa complexes via route 1. However, $Co(dmgH)_2pyCl$ at this concentration absorbs light strongly at wavelengths that overlap with the ICT absorption band of the cMa complexes (Figure S26). Thus,

the concentration of $Co(dmgH)_2pyCl$ needs be lowered to less than 1 mM to allow efficient photon absorption from the cMa complex. However, at this concentration the photosensitizer is quenched to slowly ($k_q[Q] < 2.5x10^6\ s^{-1}$) to effectively carry out the HER process. Hence, photocatalytic efficiency is best pursued under conditions where $Co(dmgH)_2pyCl$ is reduced by the cMa anion (route 2) using high concentrations of BIH, which does not absorb light in the visible part of the spectrum.

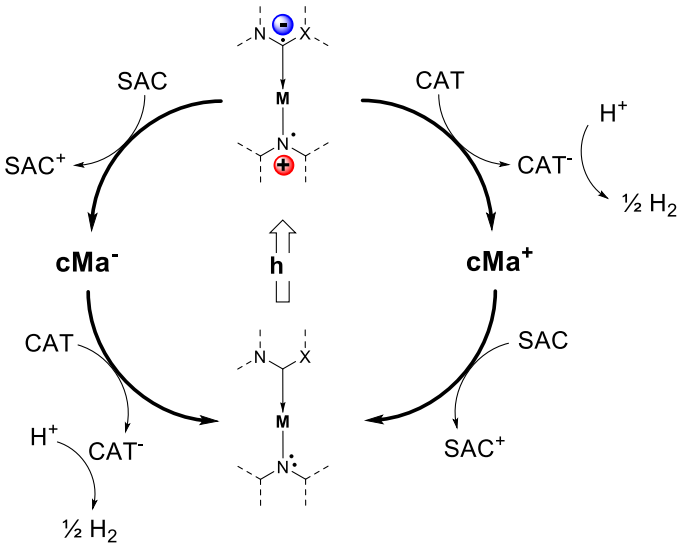

Figure 6. Schematic diagram showing two possible routes to reduce $Co(dmgH)_2pyCl$ (CAT) by the excited state of the cMa photosensitizer. Route 1 (right) involves immediate electron transfer from cMa* to the catalyst. Route 2 (left) involves immediate hole transfer from cMa* to the sacrificial reductant (SAC), followed by electron transfer from cMa^- to CAT.

Initial photo-HER experiments were performed using $Co(dmgH)_2pyCl$ (0.3 mM), BIH (200 mM) and Au_{BCz}^{MAC} as the photosensitizer in THF/water solution (5% v/v). The measured lifetime of Au_{BCz}^{MAC}* in the THF/water solution is 100 ns ($k_r + k_{nr} = 1.0x10^7\ s^{-1}$). Thus, $Co(dmgH)_2pyCl$ is expected to be reduced via route 2 under these conditions since quenching of cMa* by the cobalt-glyoxime catalyst ($k_q[Q] = 7.5x10^5\ s^{-1}$) is uncompetitive with that by BIH ($k_q[Q] = 5x10^7\ s^{-1}$). Data recorded during the first 90 minutes of irradiation with 470 nm light showed slow formation of hydrogen, giving only 1.5 turnovers based on the sensitizer (Figure 7(a)). In the next two hours the rate of hydrogen production increased significantly, eventually giving 30 turnovers at seven hours. Control experiments showed that no hydrogen was formed in the absence of the photosensitizer (Figure S21). Further, it is worth noting that protons released from BIH upon oxidation can also contribute to HER. However, irradiation of the HER system in

anhydrous THF under identical conditions for one hour produced less hydrogen (by a factor of five) than in a THF/water solution, thus confirming water as the primary source of H_2 (Figure S22).

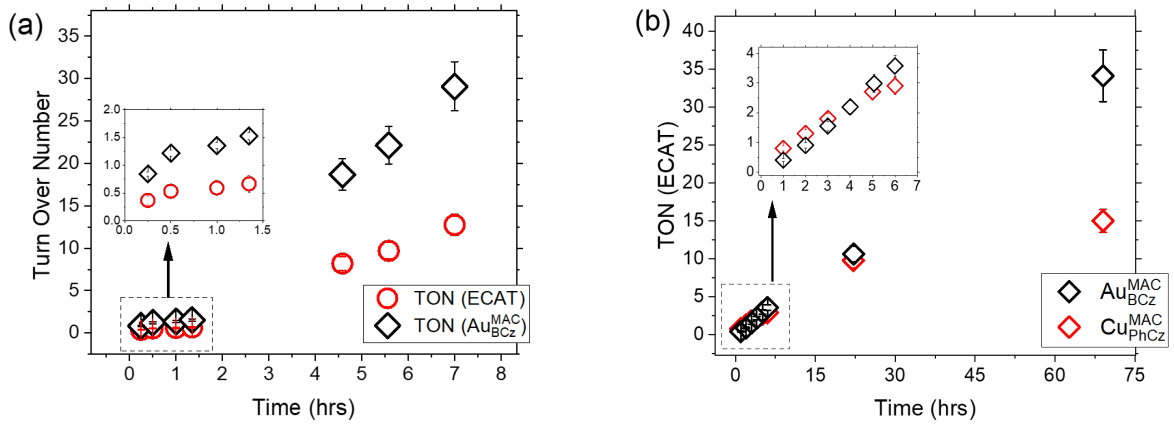

Figure 7. (a) TON versus irradiation time for Au_{BCz}^{MAC} (160 μM), $Co(dmgH)_2pyCl$ (290 μM), and BIH (200 mM) in 5 mL of the THF/water mixture (5% v/v). Turn overs are displayed with respect to the electrocatalyst (circles) or photosensitizer (diamonds). (b) Photo-HER with Au_{BCz}^{MAC} (330 μM) or Cu_{PhCz}^{MAC}(264 μM), $Co(dmgH)_2pyCl$ (300 μM), and BIH (200 mM) in the presence of 0.8 g of elemental mercury.

Interestingly, a control reaction without $Co(dmgH)_2pyCl$, *e.g.,* photolysis of only Au_{BCz}^{MAC} and BIH in THF/water, could also produce hydrogen. Hydrogen formed for the first two hours in this experiment at roughly the same rate as seen in Figure 7a, which increased before giving a TON of ~10 after 20 hours (Figure S23). A similar photolysis using Cu_{PhCz}^{MAC} showed the same behavior (~10 TON of H_2 after 20 hours, Figure S23). The presence of induction period before an increase in the rate of hydrogen production suggests that the cMa complex decomposes to form a catalytically active material during the photo-HER process. Control experiments show that the cMa complexes slowly bleach during photolysis. For example, the intensity of the ICT absorption band of Au_{BCz}^{MAC} decreased 5% upon irradiation for 9 hours with 470 nm light in THF/water (Figure S25). Decomposition of M_{BCz}^{MAC} anion after photoreduction by BIH could also be the source of the new HER catalyst. To determine if a decomposed cMa complex is solely responsible for HER, photolyses of cMa sensitizers and $Co(dmgH)_2pyCl$ in the presence of mercury were carried out, since this element has been shown to suppress catalysis from metal nanoparticles.[31] A linear increase in H_2 formation was observed at the start of the reaction under these conditions (Figure

7b). Therefore, the cMa complex does indeed photosensitize the cobalt-glyoxime catalyst, which produces H_2 in a homogeneous process. Thus, we suspect that a likely HER catalyst produced by decomposition of the sensitizer could be metal nanoparticles, which would be consistent with the observed incubation period when the Co catalyst is absent. For example, nanoparticle metal complexes containing up to thirteen gold atoms have been prepared upon reduction of $Au_{Cl}^{carbene}$ complexes with $NaBH_4$.[32] To test this hypothesis, photolyses of M_{amide}^{MAC} and BIH were performed in THF/water with the addition of elemental mercury, which led to a marked decrease in the production of H_2. Only 0.8 and 0.2 TONs, corresponding to >90% reduction in hydrogen production, was observed after ~23 hours of irradiation for Cu_{PhCz}^{MAC} and Au_{BCz}^{MAC}, respectively (Figure S24). These results suggest the intriguing possibility that the cMa complexes can also serve as a robust single component for photocatalytic HER. Both Cu_{PhCz}^{MAC} and Au_{BCz}^{MAC} promote catalytic HER in the absence of $Co(dmgH)_2pyCl$ as well, with similar performance after 22 hours of irradiation. However, the Au_{BCz}^{MAC} complex exhibits higher stability compared to Cu_{PhCz}^{MAC} as the Au derivative can drive HER at a consistent rate for over the 69 hours (~0.5 TON/hr).

Conclusion

Photophysical investigations into the excited state redox properties of two-coordinate coinage cMa complexes demonstrate that these compounds are viable as a new class of photosensitizers for production of solar fuels. Figures of merit were investigated in a variety of solvents for three two-coordinated Cu(I) and Au(I) cMa complexes. All reported complexes efficiently absorb visible light, are potent photoreducing agents and have long-lived excited states. Electrochemical studies show that substituents at the 3,6-position of carbazole stabilizes the cationic species generated upon oxidation. The Cu(I) complexes have lower molar absorptivities and electrochemical stability than the Au(I) analog, but both have comparable excited state reducing potential ($E^{+/*}$ = -2.3 V vs. $Fc^{+/0}$), which are higher than values found in commonly used photosensitizers such as $Ru(bpy)_3^{2+}$ ($E^{+/*}$ = -1.12 V vs. $Fc^{+/0}$) and $Ir(ppy)_3$ ($E^{+/*}$ = - 2.14 V vs. $Fc^{+/0}$). Two-coordinate cMa complexes also have excited state reduction potentials greater than Cu(I) bis phenanthroline systems, ($E^{+/*}$ = -1.8 V vs. $Fc^{+/0}$).[2b]

We find that the choice of carbene largely determines the value for $E^{+}/*$ in cMa complexes, while the amide determines the value for $E^{*/-}$ which is a result of the ICT nature of the excited state. The facile ability to tailor absorption and redox properties of the ICT state in two-coordinate

complexes offers enhanced tunability compared to Cu(I) complexes relying on an MLCT excited state. Two-coordinate cMa complexes can be modified to make even more potent photo-reducing agents using carbenes with more negative reduction potentials than the carbene used here; however, such a change will shift the lowest energy absorption bands into the near-UV spectrum. The ICT transitions can be shifted back into the visible spectrum by pairing these carbenes with amides that have lower oxidation potentials, thus lowering the energy of the ICT state. Alternatively, amides such as cyano-substituted carbazole can be used to increase the $E^{*/-}$ for photo-oxidative applications. Therefore, these cMa complexes can be designed to activate any given electrocatalysts with significant control over the energy of the visible absorption transition, which makes them a promising new class of photosensitizers to produce solar fuels.

This work is the first demonstration of photocatalytic HER driven by copper and gold cMa complexes, using a well-studied cobalt-glyoxime HER electrocatalyst ($Co(dmgH)_2pyCl$). We find that Au^{MAC}_{BCz} is more stable over prolonged irradiation compared to Cu^{MAC}_{PhCz}, which mirrors the added electrochemical stability of gold cMa complexes compared to copper analogues. We observe a steady, linear increase of up to 34 TON from Au^{MAC}_{BCz} upon 3 days of irradiation with a 470 nm LED, whereas Cu^{MAC}_{PhCz} plateaus at 14 TON under the same conditions. These turnover numbers are comparable to other photosensitizers when paired with the cobalt-glyoxime electrocatalyst. Copper phenanthroline systems exhibit 18 - 35 TON, and Ir/Ru/Pt systems fall between 20 – 200 with the $Co(dmgH)_2pyCl$.[23b, 23c, 27a, 33] While the turn over numbers of the two-coordinate cMas are reasonable, we anticipate much higher turnover numbers are possible. The TONs and turnover frequency can likely be significantly increased by optimizing the choice of electrocatalyst, light source, pH, and sacrificial reductant.[34]

It is important to note that in the reaction described above the cMa complex photosensitizes the HER catalyst in a homogeneous process since hydrogen is still produced in the presence of elemental mercury. However, when both cobalt-glyoxime and mercury are omitted from the system, hydrogen is still produced by either Au^{MAC}_{BCz} or Cu^{MAC}_{PhCz} at a level of *ca*. 20 turnovers after 20 hours. The fact that an induction period precedes a steep increase in HER activity in these experiments suggests that a new catalytically active species is formed during photolysis, likely metal nanoparticles. Suppression of HER activity in the cobalt-free reaction using elemental mercury provides additional evidence heterogenous electrocatalysis performed by metal

nanoparticles. Based on the work of Crudden, *et al.*,[32] we suspect that the carbene ligands remain capped to these nanoparticles. Note that the work reported here involves using cMa sensitizers that have the same carbene ligand. Therefore, we are in the process of exploring whether this "self-catalyzed" cMa based HER can be performed with cMa derivatives ligated to other carbenes, to further explore the activity and stability of the metal nanoparticle electrocatalysis.

Accession Codes

CCDC 2238026 2237840, and 2237833 contain the supplementary crystallographic data for this paper. These data can be obtained free of charge via www.ccdc.cam.ac.uk/data_request/cif, or by emailing data_request@ccdc.cam.ac.uk, or by contacting The Cambridge Crystallographic Data Centre, 12 Union Road, Cambridge CB2 1EZ, UK; fax: +44 1223 336033.

Supporting Information

Synthesis and characterization, X-ray structural data, computational details, photophysical details, electrochemical traces, excited state quenching experiments, Rehm-Weller analysis parameters, photolysis details, ^{1}H and ^{13}C NMR spectra of all reported compounds.

Author Information

Corresponding Author

Mark E. Thompson − orcid.org/0000-0002-7764-4096; Email: met@ usc.edu

Authors

Collin N. Muniz − orcid.org/0000-0003-4383-6353

Jonas Schaab − orcid.org/0000-0001-7346-9561

Peter I. Djurovich − orcid.org/0000-0001-6716-389

Author Contributions

†Authors C.N.M and C.A.A contributed equally to this work.

Acknowledgements

The authors would like to acknowledge the Department of Energy, Office of Basic Energy Science (Award: DE-SC0016450) for support. We also thank the National Science Foundation (Award: CHE-2018740) for funds used to acquire the X-ray diffractometer that was used to determine the crystal structures reported here. In addition, we thank National Science Foundation (DBI-0821671, CHE-0840366) and National Institute of Health (S10 RR25432) for funds to acquire the NMR spectrometers used in our work. We thank the Surya Prakash lab for providing access to gas chromatography facilities.

References

1. (a) Kärkäs, M. D.; Verho, O.; Johnston, E. V.; Åkermark, B., Artificial Photosynthesis: Molecular Systems for Catalytic Water Oxidation. *Chem. Rev.* **2014,** *114* (24), 11863-12001; (b) Cheung, K. P. S.; Sarkar, S.; Gevorgyan, V., Visible Light-Induced Transition Metal Catalysis. *Chem. Rev.* **2022,** *122* (2), 1543-1625.

2. (a) Bevernaegie, R.; Wehlin, S. A. M.; Piechota, E. J.; Abraham, M.; Philouze, C.; Meyer, G. J., . . . Troian-Gautier, L., Improved Visible Light Absorption of Potent Iridium(III) Photo-oxidants for Excited-State Electron Transfer Chemistry. *Journal of the American Chemical Society* **2020,** *142* (6), 2732-2737; (b) Prier, C. K.; Rankic, D. A.; MacMillan, D. W. C., Visible Light Photoredox Catalysis with Transition Metal Complexes: Applications in Organic Synthesis. *Chem. Rev.* **2013,** *113* (7), 5322-5363.

3. Larsen, C. B.; Wenger, O. S., Photoredox Catalysis with Metal Complexes Made from Earth-Abundant Elements. *Chemistry – A European Journal* **2018,** *24* (9), 2039-2058.

4. (a) Hockin, B. M.; Li, C.; Robertson, N.; Zysman-Colman, E., Photoredox catalysts based on earth-abundant metal complexes. *Catalysis Science & Technology* **2019,** *9* (4), 889-915; (b) Chan, A. Y.; Perry, I. B.; Bissonnette, N. B.; Buksh, B. F.; Edwards, G. A.; Frye, L. I., . . . MacMillan, D. W. C., Metallaphotoredox: The Merger of Photoredox and Transition Metal Catalysis. *Chem. Rev.* **2022,** *122* (2), 1485-1542; (c) Hossain, A.; Bhattacharyya, A.; Reiser, O., Copper's rapid ascent in visible-light photoredox catalysis. *Science* **2019,** *364* (6439).

5. (a) Lazorski, M. S.; Castellano, F. N., Advances in the light conversion properties of Cu(I)-based photosensitizers. *Polyhedron* **2014,** *82*, 57-70; (b) McMillin, D. R.; Buckner, M. T.; Ahn, B. T., A light-induced redox reaction of bis(2,9-dimethyl-1,10-phenanthroline)copper(I). *Inorganic Chemistry* **1977,** *16* (4), 943-945; (c) Zhang, Y.; Schulz, M.; Wächtler, M.; Karnahl, M.; Dietzek, B., Heteroleptic diimine–diphosphine Cu(I) complexes as an alternative towards noble-metal based photosensitizers: Design strategies, photophysical properties and perspective applications. *Coord. Chem. Rev.* **2018,** *356*, 127-146.

6. (a) Alkan-Zambada, M.; Hu, X., Cu Photoredox Catalysts Supported by a 4,6-Disubstituted 2,2′-Bipyridine Ligand: Application in Chlorotrifluoromethylation of Alkenes. *Organometallics* **2018,** *37* (21), 3928-3935; (b) Cuttell, D. G.; Kuang, S.-M.; Fanwick, P. E.; McMillin, D. R.; Walton, R. A., Simple Cu(I) Complexes with Unprecedented Excited-State Lifetimes. *Journal of the American Chemical Society* **2002,** *124* (1), 6-7; (c) Yu, Z.-J.; Chen, H.; Lennox, A. J. J.; Yan, L.-J.; Liu, X.-F.; Xu, D.-D., . . . Luo, S.-P., Heteroleptic copper(I) photosensitizers with carbazole-substituted phenanthroline ligands: Synthesis, photophysical properties and application to photocatalytic H2 generation. *Dyes and Pigments* **2019,** *162*, 771-775; (d) Hernandez-Perez, A. C.; Collins, S. K., Heteroleptic Cu-Based Sensitizers in Photoredox Catalysis. *Acc. Chem. Res.* **2016,** *49* (8), 1557-1565; (e) Sakaki, S.; Kuroki, T.; Hamada, T., Synthesis of a new copper(i) complex, [Cu(tmdcbpy)2]+ (tmdcbpy = 4,4′,6,6′-tetramethyl-2,2′-bipyridine-5,5′-dicarboxylic acid), and its application to solar cells. *J. Chem. Soc., Dalton Trans.* **2002,** (6), 840-842.

7. Bersuker, I. B., Pseudo-Jahn–Teller Effect—A Two-State Paradigm in Formation, Deformation, and Transformation of Molecular Systems and Solids. *Chem. Rev.* **2013,** *113* (3), 1351-1390.

8. (a) Cunningham, C. T.; Cunningham, K. L. H.; Michalec, J. F.; McMillin, D. R., Cooperative Substituent Effects on the Excited States of Copper Phenanthrolines. *Inorganic Chemistry* **1999,** *38* (20), 4388-4392; (b) Rosko, M. C.; Wells, K. A.; Hauke, C. E.; Castellano, F. N., Next Generation Cuprous Phenanthroline MLCT Photosensitizer Featuring Cyclohexyl Substituents. *Inorganic Chemistry* **2021,** *60* (12), 8394-8403; (c) Lavie-Cambot, A.; Cantuel, M.; Leydet, Y.; Jonusauskas, G.; Bassani, D. M.; McClenaghan, N. D., Improving the photophysical properties of copper(I) bis(phenanthroline) complexes. *Coord. Chem. Rev.* **2008,** *252* (23), 2572-2584; (d) Dietrich-Buchecker, C. O.; Marnot, P. A.; Sauvage, J.-P.; Kirchhoff, J. R.; McMillin, D. R., Bis(2,9-diphenyl-1,10-phenanthroline)copper(I): a copper complex with a long-lived charge-transfer excited state. *J. Chem. Soc., Chem. Commun.* **1983,** (9), 513-515; (e) Eggleston, M. K.; McMillin, D. R.; Koenig, K. S.; Pallenberg, A. J., Steric Effects in the Ground and Excited States of Cu(NN)2+ Systems. *Inorganic Chemistry* **1997,** *36* (2), 172-176.

9. (a) Muniz, C. N.; Schaab, J.; Razgoniaev, A.; Djurovich, P. I.; Thompson, M. E., π-Extended Ligands in Two-Coordinate Coinage Metal Complexes. *Journal of the American Chemical Society* **2022,** *144* (39), 17916-17928; (b) Hamze, R.; Peltier, J. L.; Sylvinson, D.; Jung, M.; Cardenas, J.; Haiges, R., . . . Thompson, M. E., Eliminating nonradiative decay in Cu(I) emitters: >99% quantum efficiency and microsecond lifetime. *Science* **2019,** *363* (6427), 601; (c) Hamze, R.; Idris, M.; Muthiah Ravinson, D. S.; Jung, M. C.; Haiges, R.; Djurovich, P. I.; Thompson, M. E., Highly Efficient Deep Blue Luminescence of 2-Coordinate Coinage Metal Complexes Bearing Bulky NHC Benzimidazolyl Carbene. *Frontiers in Chemistry* **2020,** *8*, 401; (d) Shi, S.; Jung, M. C.; Coburn, C.; Tadle, A.; Sylvinson M. R, D.; Djurovich, P. I., . . . Thompson, M. E., Highly Efficient Photo- and Electroluminescence from Two-Coordinate Cu(I) Complexes Featuring Nonconventional N-Heterocyclic Carbenes. *Journal of the American Chemical Society* **2019,** *141* (8), 3576-3588; (e) Hamze, R.; Shi, S.; Kapper, S. C.; Muthiah Ravinson, D. S.; Estergreen, L.; Jung, M.-C., . . . Thompson, M. E., "Quick-Silver" from a Systematic Study of Highly Luminescent, Two-Coordinate, d10 Coinage Metal Complexes. *Journal of the American Chemical Society* **2019,** *141* (21), 8616-8626; (f) Yang, J.-G.; Song, X.-F.; Cheng, G.; Wu, S.; Feng, X.; Cui, G., . . . Li, K., Conformational Engineering of Two-Coordinate Gold(I) Complexes: Regulation of Excited-State Dynamics for Efficient Delayed Fluorescence. *ACS Applied Materials & Interfaces* **2022,** *14* (11), 13539-13549; (g) Tang, R.; Xu, S.; Lam, T.-L.; Cheng, G.; Du, L.; Wan, Q., . . . Che, C.-M., Highly Robust CuI-TADF Emitters for Vacuum-Deposited OLEDs with Luminance up to 222 200 cd m−2 and Device Lifetimes (LT90) up to 1300 hours at an Initial Luminance of 1000 cd m−2. *Angew. Chem. Int. Ed.* **2022,** *61* (33), e202203982; (h) Bertrand, B.; Romanov, A. S.; Brooks, M.; Davis, J.; Schmidt, C.; Ott, I., . . . Bochmann, M., Synthesis, structure and cytotoxicity of cyclic (alkyl)(amino) carbene and acyclic carbene complexes of group 11 metals. *Dalton Transactions* **2017,** *46* (45), 15875-15887; (i) Chotard, F.; Sivchik, V.; Linnolahti, M.; Bochmann, M.; Romanov, A. S., Mono- versus Bicyclic Carbene Metal Amide Photoemitters: Which Design Leads to the Best Performance? *Chem. Mater.* **2020,** *32* (14),

6114-6122; (j) Conaghan, P. J.; Matthews, C. S. B.; Chotard, F.; Jones, S. T. E.; Greenham, N. C.; Bochmann, M., . . . Romanov, A. S., Highly efficient blue organic light-emitting diodes based on carbene-metal-amides. *Nature Communications* **2020,** *11* (1), 1758; (k) Gernert, M.; Balles-Wolf, L.; Kerner, F.; Müller, U.; Schmiedel, A.; Holzapfel, M., . . . Steffen, A., Cyclic (Amino)(aryl)carbenes Enter the Field of Chromophore Ligands: Expanded π System Leads to Unusually Deep Red Emitting CuI Compounds. *Journal of the American Chemical Society* **2020,** *142* (19), 8897-8909.

10. Romanov, A. S.; Jones, S. T. E.; Gu, Q.; Conaghan, P. J.; Drummond, B. H.; Feng, J., . . . Bochmann, M., Carbene metal amide photoemitters: tailoring conformationally flexible amides for full color range emissions including white-emitting OLED. *Chemical Science* **2020,** *11* (2), 435-446.

11. McCusker, C. E.; Castellano, F. N., Design of a Long-Lifetime, Earth-Abundant, Aqueous Compatible Cu(I) Photosensitizer Using Cooperative Steric Effects. *Inorganic Chemistry* **2013,** *52* (14), 8114-8120.

12. Karon, K.; Lapkowski, M., Carbazole electrochemistry: a short review. *J. Solid State Electrochem.* **2015,** *19* (9), 2601-2610.

13. Epifanovsky, E.; Gilbert, A. T. B.; Feng, X.; Lee, J.; Mao, Y.; Mardirossian, N., . . . Krylov, A. I., Software for the frontiers of quantum chemistry: An overview of developments in the Q-Chem 5 package. *The Journal of Chemical Physics* **2021,** *155* (8), 084801.

14. Lu, T.; Chen, F., Multiwfn: A multifunctional wavefunction analyzer. *J. Comput. Chem.* **2012,** *33* (5), 580-592.

15. Liebeskind, L. S.; Leeds, J. P.; Baysdon, S. L.; Iyer, S., Convergent, high-yield, regioselective synthesis of substituted benzoquinones from maleoylcobalt complexes and alkynes. *Journal of the American Chemical Society* **1984,** *106* (21), 6451-6453.

16. Hou, S.; Yang, H.; Cheng, B.; Zhai, H.; Li, Y., Cobaloxime-catalyzed hydration of terminal alkynes without acidic promoters. *Chem. Commun.* **2017,** *53* (51), 6926-6929.

17. Föller, J.; Marian, C. M., Rotationally Assisted Spin-State Inversion in Carbene–Metal–Amides Is an Artifact. *The Journal of Physical Chemistry Letters* **2017,** *8* (22), 5643-5647.

18. (a) Wang, H.-J.; Liu, Y.; Yu, B.; Song, S.-Q.; Zheng, Y.-X.; Liu, K., . . . Li, T.-Y., A Configurationally Confined Thermally Activated Delayed Fluorescent Two-Coordinate CuI Complex for Efficient Blue Electroluminescence. *Angew. Chem. Int. Ed.* **2023,** *62* (7), e202217195; (b) Gu, Q.; Chotard, F.; Eng, J.; Reponen, A.-P. M.; Vitorica-Yrezabal, I. J.; Woodward, A. W., . . . Romanov, A. S., Excited-State Lifetime Modulation by Twisted and Tilted Molecular Design in Carbene-Metal-Amide Photoemitters. *Chem. Mater.* **2022,** *34* (16), 7526-7542.

19. Neogrdy, P.; Kell, V.; Urban, M.; Sadlej, A. J., Ionization potentials and electron affinities of Cu, Ag, and Au: Electron correlation and relativistic effects. *International Journal of Quantum Chemistry* **1997,** *63* (2), 557-565.

20. Li, T.-y.; Schaab, J.; Djurovich, P. I.; Thompson, M. E., Toward rational design of TADF two-coordinate coinage metal complexes: understanding the relationship between natural transition orbital overlap and photophysical properties. *Journal of Materials Chemistry C* **2022,** *10* (12), 4674-4683.

21. (a) Pellegrin, Y.; Sandroni, M.; Blart, E.; Planchat, A.; Evain, M.; Bera, N. C., . . . Odobel, F., New Heteroleptic Bis-Phenanthroline Copper(I) Complexes with Dipyridophenazine or Imidazole Fused Phenanthroline Ligands: Spectral, Electrochemical, and Quantum Chemical Studies. *Inorganic Chemistry* **2011,** *50* (22), 11309-11322; (b) Ruthkosky, M.; Castellano, F. N.; Meyer, G. J., Photodriven Electron and Energy Transfer from Copper Phenanthroline Excited States. *Inorganic Chemistry* **1996,** *35* (22), 6406-6412; (c) Das, S.; Rodrigues, R. R.; Lamb, R. W.; Qu, F.; Reinheimer, E.; Boudreaux, C. M., . . . Papish, E. T., Highly Active Ruthenium CNC Pincer Photocatalysts for Visible-Light-Driven Carbon Dioxide Reduction. *Inorganic Chemistry* **2019,** *58* (12), 8012-8020; (d) Huckaba, A. J.; Shirley, H.; Lamb, R. W.; Guertin, S.; Autry, S.; Cheema, H., . . . Delcamp, J. H., A Mononuclear Tungsten Photocatalyst for H2 Production. *ACS Catalysis* **2018,** *8* (6), 4838-4847; (e) Tinker, L. L.; Bernhard, S., Photon-Driven Catalytic Proton Reduction with a Robust Homoleptic Iridium(III) 6-Phenyl-2,2′-bipyridine Complex ([Ir(C^N^N)2]+). *Inorganic Chemistry* **2009,** *48* (22), 10507-10511.

22. (a) Ma, B.; Djurovich, P.; Thompson, M., Excimer and electron transfer quenching studies of a cyclometalated platinum complex. *Coord. Chem. Rev.* **2005,** *249*, 1501-1510; (b) Rosspeintner, A.; Kattnig, D. R.; Angulo, G.; Landgraf, S.; Grampp, G., The Rehm–Weller Experiment in View of Distant Electron Transfer. *Chemistry – A European Journal* **2008,** *14* (20), 6213-6221; (c) Fukuzumi, S.; Fujita, M.; Otera, J.; Fujita, Y., Electron-transfer oxidation of ketene silyl acetals and other organosilanes. Mechanistic insight into Lewis acid mediated electron transfer. *Journal of the American Chemical Society* **1992,** *114* (26), 10271-10278.

23. (a) Fischer, S.; Rösel, A.; Kammer, A.; Barsch, E.; Schoch, R.; Junge, H., . . . Ludwig, R., Diferrate [Fe2(CO)6(μ-CO){μ-P(aryl)2}]− as Self-Assembling Iron/Phosphor-Based Catalyst for the Hydrogen Evolution Reaction in Photocatalytic Proton Reduction—Spectroscopic Insights. *Chemistry – A European Journal* **2018,** *24* (60), 16052-16065; (b) Natali, M., Elucidating the Key Role of pH on Light-Driven Hydrogen Evolution by a Molecular Cobalt Catalyst. *ACS Catalysis* **2017,** *7* (2), 1330-1339; (c) Khnayzer, R. S.; McCusker, C. E.; Olaiya, B. S.; Castellano, F. N., Robust Cuprous Phenanthroline Sensitizer for Solar Hydrogen Photocatalysis. *Journal of the American Chemical Society* **2013,** *135* (38), 14068-14070.

24. Jones, W. E., Jr.; Fox, M. A., Determination of Excited-State Redox Potentials by Phase-Modulated Voltammetry. *The Journal of Physical Chemistry* **1994,** *98* (19), 5095-5099.

25. Scandola, F.; Balzani, V., Free-energy relationships for electron-transfer processes. *Journal of the American Chemical Society* **1979,** *101* (20), 6140-6142.

26. Rehm, D.; Weller, A., Kinetics of Fluorescence Quenching by Electron and H-Atom Transfer. *Isr. J. Chem.* **1970,** *8* (2), 259-271.

27. (a) Khnayzer, R. S.; Olaiya, B. S.; El Roz, K. A.; Castellano, F. N., Homogeneous Photocatalytic H2 Production Using a RuII Bathophenanthroline Metal-to-Ligand Charge-Transfer Photosensitizer. *ChemPlusChem* **2016,** *81* (10), 1016-1016; (b) O'Neill, J. S.; Kearney, L.; Brandon, M. P.; Pryce, M. T., Design components of porphyrin-based photocatalytic hydrogen evolution systems: A review. *Coord. Chem. Rev.* **2022,** *467*, 214599; (c) Robertson, W. D.; Bovell, A. M.; Warncke, K., Cobinamide production of hydrogen in a homogeneous aqueous photochemical system, and assembly and photoreduction in a (βα)8 protein. *JBIC Journal of Biological Inorganic Chemistry* **2013,** *18* (6), 701-713; (d) Lazarides, T.; McCormick, T.; Du, P.; Luo, G.; Lindley, B.; Eisenberg, R., Making Hydrogen from Water Using a Homogeneous System Without Noble Metals. *Journal of the American Chemical Society* **2009,** *131* (26), 9192-9194.

28. Dempsey, J. L.; Brunschwig, B. S.; Winkler, J. R.; Gray, H. B., Hydrogen Evolution Catalyzed by Cobaloximes. *Acc. Chem. Res.* **2009,** *42* (12), 1995-2004.

29. (a) Hasegawa, E.; Takizawa, S.; Seida, T.; Yamaguchi, A.; Yamaguchi, N.; Chiba, N., . . . Akiyama, K., Photoinduced electron-transfer systems consisting of electron-donating pyrenes or anthracenes and benzimidazolines for reductive transformation of carbonyl compounds. *Tetrahedron* **2006,** *62* (27), 6581-6588; (b) Pellegrin, Y.; Odobel, F., Sacrificial electron donor reagents for solar fuel production. *Comptes Rendus Chimie* **2017,** *20* (3), 283-295.

30. Kellogg1, M. S.; Mencke, A. R.; Muniz, C. N.; Thabassum, A. N. K.; Cardoso-Delgado, F.; Baluyot-Reyes, N., . . . Thompson, M. E., Intra- and Inter-Molecular Charge Transfer Dynamics of Carbene-Metal-Amide Photosensitizers. *ChemRxiv (https://chemrxiv.org/)* **2023**, DOI: 10.26434/chemrxiv-2023-6tqv9.

31. Wang, X.; Goeb, S.; Ji, Z.; Pogulaichenko, N. A.; Castellano, F. N., Homogeneous photocatalytic hydrogen production using π-conjugated platinum (II) arylacetylide sensitizers. *Inorganic chemistry* **2011,** *50* (3), 705-707.

32. Narouz, M. R.; Takano, S.; Lummis, P. A.; Levchenko, T. I.; Nazemi, A.; Kaappa, S., . . . Crudden, C. M., Robust, Highly Luminescent Au(13) Superatoms Protected by N-Heterocyclic Carbenes. *J. Am. Chem. Soc.* **2019,** *141* (38), 14997-15002.

33. (a) Windisch, J.; Orazietti, M.; Hamm, P.; Alberto, R.; Probst, B., General Scheme for Oxidative Quenching of a Copper Bis-Phenanthroline Photosensitizer for Light-Driven Hydrogen Production. *ChemSusChem* **2016,** *9* (13), 1719-1726; (b) Yang, M.; Yarnell, J. E.; El Roz, K.; Castellano, F. N., A Robust Visible-Light-Harvesting Cyclometalated Ir(III) Diimine Sensitizer for Homogeneous Photocatalytic Hydrogen Production. *ACS Applied Energy Materials* **2020,** *3* (2), 1842-1853; (c) Guo, S.; Chen, K.-K.; Dong, R.; Zhang, Z.-M.; Zhao, J.; Lu, T.-B., Robust and Long-Lived Excited State Ru(II) Polyimine Photosensitizers Boost Hydrogen Production. *ACS Catalysis* **2018,** *8* (9), 8659-8670; (d) Wang, X.; Goeb, S.; Ji, Z.; Pogulaichenko, N. A.; Castellano, F. N., Homogeneous Photocatalytic Hydrogen Production Using π-Conjugated Platinum(II) Arylacetylide Sensitizers. *Inorganic Chemistry* **2011,** *50* (3), 705-707.

34. (a) Kohler, L.; Niklas, J.; Johnson, R. C.; Zeller, M.; Poluektov, O. G.; Mulfort, K. L., Molecular cobalt catalysts for H2 generation with redox activity and proton relays in the second coordination sphere. *Inorganic Chemistry* **2018,** *58* (2), 1697-1709; (b) Barrozo, A.; Orio, M., Molecular electrocatalysts for the hydrogen evolution reaction: input from quantum chemistry. *ChemSusChem* **2019,** *12* (22), 4905-4915; (c) Xie, L.; Tian, J.; Ouyang, Y.; Guo, X.; Zhang, W.; Apfel, U.-P., . . . Cao, R., Water-Soluble Polymers with Appending Porphyrins as Bioinspired Catalysts for the Hydrogen Evolution Reaction. *Angew. Chem. Int. Ed.* **2020,** *59* (37), 15844-15848.

Supporting Information

Two-Coordinate Coinage Metal Complexes as Solar Photosensitizers

Collin N. Muniz,[†] Claire A. Archer,[†] Jack S. Applebaum, Anushan Alagaratnam, Jonas Schaab, Peter I. Djurovich, Mark E. Thompson[*]

Department of Chemistry, University of Southern California, Los Angeles, CA 90089

Table of Contents

Synthesis and Characterization 4

Scheme S1. Synthesis of cMa photosensitizers 4

Synthesis of 1,3-bis(2,6-diisopropylphenyl)-5,5-dimethyl-4-oxo-3,4,5,6-tetrahydropyrimidin-1-ium-2-ide-Cu(I)-3,6-di-tert-butylcarbazol-9-ide ($\mathbf{Cu}_{\mathbf{BCZ}}^{\mathbf{MAC}}$): 4

Synthesis of 1,3-bis(2,6-diisopropylphenyl)-5,5-dimethyl-4-oxo-3,4,5,6-tetrahydropyrimidin-1-ium-2-ide-Cu(I)-3,6-di-phenylcarbazol-9-ide ($\mathbf{Cu}_{\mathbf{PhCZ}}^{\mathbf{MAC}}$): 4

Synthesis of 1,3-bis(2,6-diisopropylphenyl)-5,5-dimethyl-4-oxo-3,4,5,6-tetrahydropyrimidin-1-ium-2-ide-Au(I)-3,6-di-tert-butylcarbazol-9-ide ($\mathbf{Au}_{\mathbf{BCZ}}^{\mathbf{MC}}$): 5

Crystal Structures 5

Figure S1. Single crystal structures of all new cMa complexes 6

Table S1: Selected bond lengths and angles for the(carbene)M(amide) complexes. 6

Table S2. Crystallographic Parameters for $\mathbf{Cu}_{\mathbf{BCZ}}^{\mathbf{MAC}}$, $\mathbf{Au}_{\mathbf{BCZ}}^{\mathbf{MAC}}$ and $\mathbf{Cu}_{\mathbf{PhCZ}}^{\mathbf{MAC}}$ 7

Computation 8

Figure S2. HOMO and LUMO densities of all reported photosensitizers. 8

Table S3. The percent contribution of the gold atom of $\mathbf{Au}_{\mathbf{BCZ}}^{\mathbf{MAC}}$ to the HOMO and LUMO 8

Photophysics 9

Figure S3. Custom Schlenk cuvettes 9

Figure S4. Molar absorptivity spectra in THF 10

Figure S5. Solvent dependent PL of $\mathbf{Cu}_{\mathbf{BCZ}}^{\mathbf{MAC}}$ 10

Figure S6. Solvent dependent PL of $\mathbf{Au}_{\mathbf{BCZ}}^{\mathbf{MAC}}$ 11

Figure S7. Solvent dependent PL of $\mathbf{Cu}_{\mathbf{PhCZ}}^{\mathbf{MAC}}$ 11

Table S4. Photophysical parameters of all reported complexes in toluene, THF, CH_2Cl_2, DMF, and MeCN. 12

Figure S8. The non-radiative rate vs. solvent $E_T(30)$ 13

Electrochemistry 14

Figure S9. CV and DPV measurements of all reported compounds in DMF vs. $Fc^{+/0}$. 14

Figure S10. CV and DPV measurements of all reported compounds in MeCN vs. $Fc^{+/0}$. 15

Figure S11. CV and DPV measurements of all reported compounds in THF vs. $Fc^{+/0}$. 16

Figure S12. CV measurements of the first oxidation in DCM vs. $Fc^{+/0}$ 17

Table S5. Electrochemical potentials of cMa complexes in various solvents 18

Figure S13. Reductive DPV sweep of electron accepting quenchers 18

Figure S14. DPV of $Co(dmgH)_2pyCl$ in DMF 19

Excited State Quenching 19

Figure S15. Stern-Volmer plots measured in THF 20

Figure S16. Stern-Volmer plots measured in toluene. 21

Figure S17. Stern-Volmer plots measured in MeCN. 22

Table S6. Stern-Volmer results of k_q in toluene 22

Table S7. Stern-Volmer results of k_q in MeCN 22

Table S8. Parameters from Rehm-Weller fit of k_q vs. $E^{0/-}$ 23

Photocatalysis 25

Figure S18. Experimental Setup for photocatalysis**.** 25

Figure S19. GC H_2 calibration curve 25

Figure S20. Stern-Volmer study of $\mathbf{Au}_{\mathbf{BCZ}}^{\mathbf{MAC}}$ quenched by $Co(dmgH)_2pyCl$ 26

Figure S21. Irradiation of the sample with (left) and without (right) the photosensitizer 26

Figure S22. Control experiment of photo driven HER with and without water 27

Figure S23. Photocatalysis without $Co(dmgH)_2pyCl$..... 27

Figure S24. Mercury poisoning tests after ~23 hrs of irradiation 28

Figure S25. Photostability of $\mathbf{Au}_{\mathbf{BCZ}}^{\mathbf{MAC}}$ 28

Figure S26. Absorption spectrum of a saturated $Co(dmgH)_2pyCl$..... 29

NMR 30

^1H and ^{13}C NMR Spectra 30

Figure S26. ^1H and ^{13}C NMR of $\mathbf{Cu}_{\mathbf{BCZ}}^{\mathbf{MAC}}$ in acetone-d6 30

Figure S27. ^1H and ^{13}C NMR of $\mathbf{Cu}_{\mathbf{PhCZ}}^{\mathbf{MAC}}$ in acetone-d6 31

Figure S28. ^1H and ^{13}C NMR of $\mathbf{Au}_{\mathbf{BCZ}}^{\mathbf{MAC}}$ in acetone-d6 32

Synthesis and Characterization

Scheme S1. Synthesis of cMa photosensitizers [R = tert-butyl (B) or phenyl (Ph)].

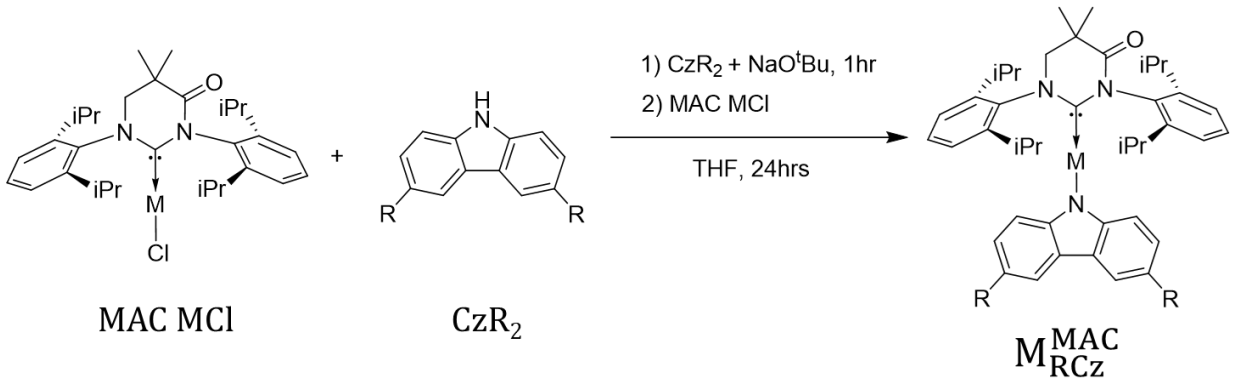

Synthesis of 1,3-bis(2,6-diisopropylphenyl)-5,5-dimethyl-4-oxo-3,4,5,6-tetrahydropyrimidin-1-ium-2-ide-Cu(I)-3,6-di-tert-butylcarbazol-9-ide ($\mathbf{Cu^{MAC}_{BCz}}$): Following the general procedure, a 150 mL Schlenk flask was charged with 512 mg 3,6-di-tert-butyl-9-H-carbazole (1.83 mols) and 185 mg sodium tert-butoxide (1.92 mols). The solids were dissolved in 80 mL THF, and 1.0 g (1.83 mols) of MAC CuCl was added. The workup yielded a yellow powder. The powder was washed with methanol which dissolved some product but removed all remaining impurities, yielding 890 mg (64% yield) of Cu^{MAC}_{BCz} as a yellow powder which is bright yellow emissive under 365 nm UV radiation. ^{1}H NMR (400 MHz, acetone-d6) δ: 7.81-7.72 (m,4H), 7.58 (d, J = 7.6 Hz, 2H), 7.52 (d, J = 7.9 Hz, 2H), 6.90 (dd, J = 8.6 Hz, 2.1 Hz, 2H), 5.52 (d, J = 8.8 Hz, 2H), 4.25 (s, 2H), 3.55 (hept, J = 7.0 Hz, 2H), 3.29 (hept, J = 7.2 Hz, 2H), 1.66 (s, 6H), 1.42 (d, J = 6.8 Hz, 6H), 1.32 (s, 18H), 1.28-1.22 (m, 18H). ^{13}C NMR (100 MHz, acetone-d6) δ: 211.0, 206.3, 206.3, 172.3, 149.5, 147.4, 146.4, 141.5, 138.0, 137.5, 131.3, 130.9, 126.7, 125.8, 124.9, 121.2, 115.3, 115.0, 62.2, 39.0, 35.0, 32.8, 32.5, 30.6, 30.4, 30.2, 30.0, 29.8, 29.8, 29.6, 29.5, 29.4, 25.5, 24.9, 24.7, 24.6, 24.5. CHN (C: 76.61%; H: 8.40%; N: 5.47%; calculated: C: 76.15%; H: 8.44%; N: 5.33%).

Synthesis of 1,3-bis(2,6-diisopropylphenyl)-5,5-dimethyl-4-oxo-3,4,5,6-tetrahydropyrimidin-1-ium-2-ide-Cu(I)-3,6-di-phenylcarbazol-9-ide ($\mathbf{Cu^{MAC}_{PhCz}}$): Following the general procedure, a 250 mL Schlenk flask was charged with 585 mg 3,6-diphenyl-9-H-carbazole (1.83 mols) and 185 mg (1.92 mols) NaO^tBu. The solids were dissolved in 100 mL THF, and 1.0 g

(1.83 mols) of MAC CuCl was added to yield a light yellow powder after the general workup. The powder was washed copiously with with diethyl ether to afford 1020 mg (67% yield) of Cu_{PhCz}^{MAC} as a shiny yellow powder which emits intense turquoise under 365 nm UV radiation. (400 MHz, acetone-d6) δ: 8.17 (dd, J = 0.7Hz, 2.0 Hz, 2H), 7.87-7.80 (m, 2H), 7.67-7.62 (m, 6H), 7.58 (d, J = 7.8 Hz, 2H), 7.41-7.36 (m, 4H), 7.23-7.18 (m, 4H), 5.66 (dd, J = 0.6 Hz, J = 8.3Hz), 4.30 (s, 2H), 3.59 (hept, J = 6.9Hz, 2H), 3.33 (hept, J = 7.0 Hz, 2H), 1.68 (s, 6H), 1.4 (d, J=6.6 Hz, 6H), 1.33-1.24 (m, 18H). ^{13}C NMR (100 MHz, acetone-d6) δ: 210.7, 206.3, 206.3, 206.3, 172.3, 151.2, 147.5, 146.4, 144.2, 141.5, 137.5, 131.5, 131.1, 129.8, 129.5, 129.4, 127.9, 127.5, 127.3, 126.8, 126.2, 126.1, 125.9, 125.9, 123.5, 119.7, 118.2, 116.1, 62.1, 39.0, 32.4, 30.5, 30.4, 30.3, 30.2, 30.0, 29.8, 29.6, 29.5, 29.4, 29.3, 25.5, 24.9, 24.7, 24.5. CHN (C: 77.70%; H: 6.94%; N: 5.14%; calculated: C: 78.27%; H: 7.06%; N: 5.07%)

Synthesis of 1,3-bis(2,6-diisopropylphenyl)-5,5-dimethyl-4-oxo-3,4,5,6-tetrahydropyrimidin-1-ium-2-ide-Au(I)-3,6-di-tert-butylcarbazol-9-ide ($\mathbf{Au_{BCz}^{MAC}}$): Following the general procedure, a 250 mL Schlenk flask was charged with 411 mg (1.47 mols) 3,6-di-tertbutyl-9-H-carbazole and 142 mg NaO^{t}Bu (1.62 mols). The solids were dissolved in 120 mL THF and 1.0g (1.47 mols) MAC AuCl was added. The general workup afforded 425 mg (31% yield) of Au_{BCz}^{MAC}as a mustard yellow powder that emits bright yellow under 365 nm radiation. ^{1}H NMR (400 MHz, acetone-d6) δ: 7.83 (d, J = 2 Hz, 2H), 7.78-7.69 (m, 2H), 7.56 (d, J = 7.7 Hz, 2H), 7.50 (d, J = 7.8 Hz, 2H), 7.0 (dd, J = 1.7 Hz, J = 9.0 Hz, 2H), 6.00 (d, J = 8.6 Hz, 2H), 4.25 (s, 2H), 3.50 (hept, J = 6.8 Hz, 2H), 3.25 (hept, J = 6.8 Hz, 2H), 1.68 (s, 6H), 1.41 (d, J = 6.7 Hz, 6H), 1.37 (d, J = 6.8 Hz, 6H), 1.34 (d, J = 7.4 Hz, 6H), 1.33 (s, 18H), 1.22 (d, J = 6.8 Hz, 6H). ^{13}C NMR (100 MHz, acetone-d6) δ 206.3, 206.3, 206.2, 205.7, 173.0, 149.1, 147.4, 146.2, 141.7, 138.8, 137.7, 131.1, 130.8, 126.4, 125.4, 124.7, 121.5, 115.5, 114.4, 62.1, 39.1, 35.0, 35.0, 32.8, 32.6, 30.6, 30.6, 30.4, 30.4, 30.2, 30.0, 29.8, 29.8, 29.6, 29.6, 29.4, 25.0, 24.7, 24.7, 24.6, 24.3, 14.8. CHN (C: 64.59%; H: 7.10%; N: 4.63%; calculated: C: 65.13%; H: 7.22%; N: 4.56%).

Crystal Structures

All crystals were grown by recrystallization. Vapor diffusion of hexanes or pentane into a solution of NMR-pure compound in DCM or Acetone. A Cryo-Loop was used to mount the sample with Paratone oil.

All single crystal structures were determined at 100K with Rigaku Xta LAB Synergy S, equipped with an HyPix-600HE detector and an Oxford Cryostream 800 low Temperature unit, using Cu K_α PhotonJet-S X-ray source. The frames were integrated using the SAINT algorithm to give the hkl files. The data was corrected for absorption effects using the multi-scan method (SADABS) with Rigaku CrysalisPro. The structures were solved by intrinsic phasing and refined with the SHELXTL Software Package. If necessary, the disordered solvent treatment method BYPASS, for co-crystalizing solvent molecules, was implemented and marked in the CCDC entry.

All cif files and crystallographic data including atom position, bond lengths and bond angle can be downloaded from the CCDC database, using the database number in the right column of Table S1 following table. Furthermore Table 1 provides the most important bond lengths, bond angles and the torsion angle around the metal center. The conformer ratio represents the ratio of two different disordered conformations of the molecule. All complexes crystalized with one molecule in the asymmetric unit.

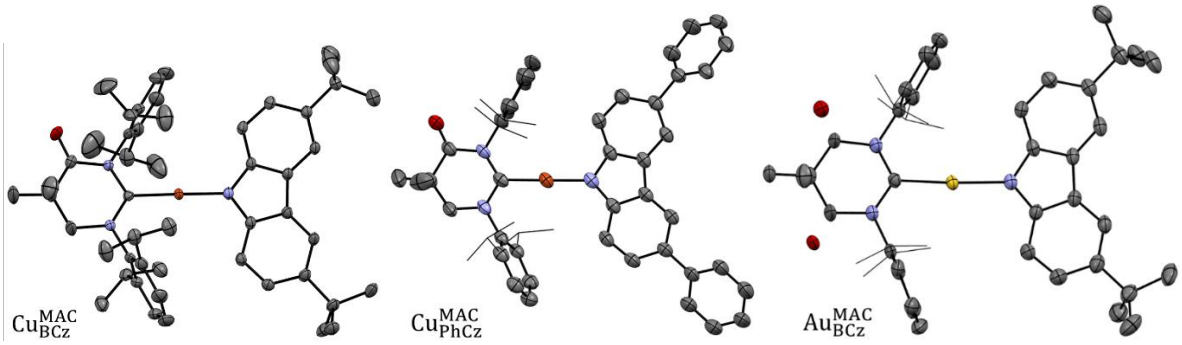

Figure S1. Single crystal structures of all new cMa complexes.

Table S1: Selected bond lengths and angles for the(carbene)M(amide) complexes.

compound	C-M (A)	M-N (A)	C-M-N (˚)	Torsion (˚) NC-M-NC	C-N-C(O) (˚) C-N-C(H_2) (˚)	Disorder ratio
Cu^{MAC}_{BCz}	1.875(2)	1.849(2)	178.71	19.62	126.41 124.03	-/-
Au^{MAC}_{BCz}	1.977(4)	1.997(3)	176.23	14.66	124.76 124.03	60/40 (CH_3) 50/50 (C=O)
Cu^{MAC}_{PhCz}	1.882(2)	1.854(2)	175.11	2.22 6.52	125.89 123.46	-/-

Table S2. Crystallographic Parameters for Cu_{BCz}^{MAC}, Au_{BCz}^{MAC} and Cu_{PhCz}^{MAC}

Identification code	$\mathbf{Cu_{BCz}^{MAC}}$	$\mathbf{Au_{BCz}^{MAC}}$	$\mathbf{Cu_{PhCz}^{MAC}}$
Empirical formula	$C_{50}H_{66}CuN_3O$	$C_{50}H_{66}AuN_3O$	$C_{54}H_{58}CuN_3O$
Formula weight	788.59	921.07	828.57
Temperature/K	99.9(3)	100.0(2)	100.0(3)
Crystal system	monoclinic	monoclinic	monoclinic
Space group	$P2_1/n$	$P2_1/n$	$P2_1/c$
a/Å	12.6232(1)	14.7369(2)	17.0684(4)
b/Å	15.5893(1)	13.0901(2)	15.5735(3)
c/Å	23.7886(2)	24.4764(4)	19.4670(4)
α/°	90	90	90
β/°	99.598(1)	107.306(2)	114.062(3)
γ/°	90	90	90
Volume/$Å^3$	4615.75(6)	4507.93(13)	4725.0(2)
Z	4	4	4
$\rho_{calc}g/cm^3$	1.135	1.357	1.165
μ/mm^{-1}	0.939	6.412	0.947
F(000)	1696.0	1892.0	1760.0
Crystal size/mm^3	0.162 × 0.216 × 0.326	0.474 × 0.294 × 0.208	0.141 × 0.089 × 0.07
Radiation	Cu Kα (λ = 1.54184)	Cu Kα (λ = 1.54184)	Cu Kα (λ = 1.54184)
2Θ range for data coll./°	6.808 to 154.728	7.566 to 154.978	5.67 to 154.09
Index ranges	$-14 \le h \le 15$, $-19 \le k \le 19$, $-28 \le l \le 30$	$-18 \le h \le 17$, $-15 \le k \le 16$, $-28 \le l \le 30$	$-20 \le h \le 14$, $-18 \le k \le 18$, $-24 \le l \le 23$
Reflections collected	85783	46425	33322
Independent reflections	9360 [R_{int} = 0.0466, R_{sigma} = 0.0214]	8765 [R_{int} = 0.0607, R_{sigma} = 0.0378]	8414 [R_{int} = 0.0451, R_{sigma} = 0.0326]
Data/restraints/parameters	9360/0/512	8765/0/544	8414/0/543
Goodness-of-fit on F^2	1.047	1.027	1.049
Final R indexes [I>=2σ]	R_1= 0.0578, wR_2= 0.1607	R_1= 0.0331, wR_2= 0.0821	R_1= 0.0581, wR_2= 0.1497
Final R indexes [all data]	R_1= 0.0624, wR_2= 0.1648	R_1 = 0.0376, wR_2 = 0.0853	R_1 = 0.0658, wR_2 = 0.1547
Largest diff. peak/hole/e $Å^{-3}$	2.29/-0.69	0.84/-1.67	0.43/-0.84
#CCDC	**2238026**	**2237840**	**2237833**

Computation

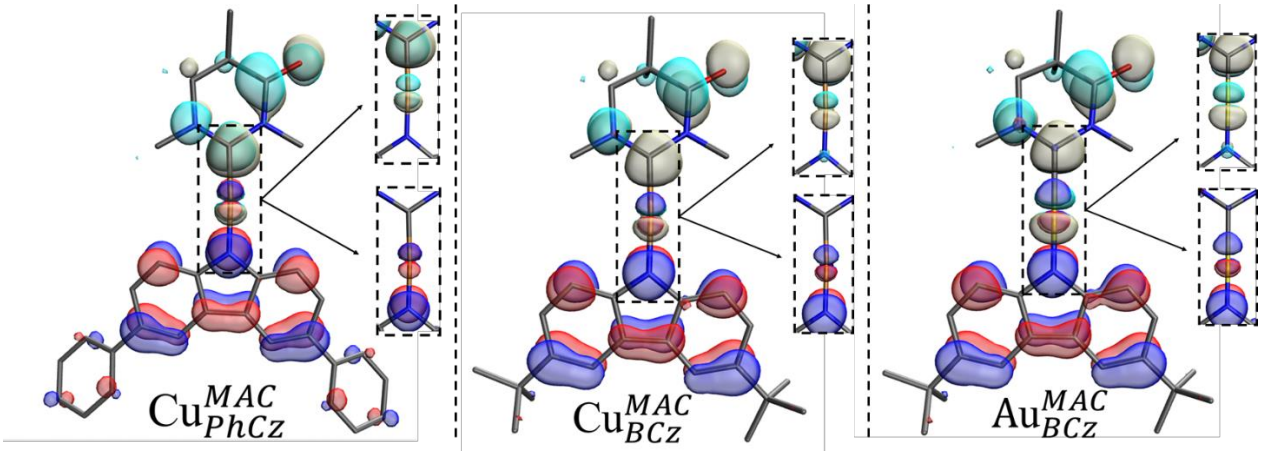

Figure S2. HOMO and LUMO densities of all reported photosensitizers. The HOMO is displayed in red and blue, and the LUMO is displayed in cyan and cream for Cu_{PhCz}^{MAC}, Cu_{BCz}^{MAC}, and Au_{BCz}^{MAC} (iso-value = 0.1). A zoomed in panel is shown for each compound to illustrate that the HOMO and LUMO wavefunctions share density at the metal center. The 3,6-diisopropylphenyl substituents, and hydrogen atoms are deleted for clarity.

Several different methods were used to evaluate the atomic orbital contribution to a given molecular orbital including the Mulliken partition method, the Stout-Politzer partition method, the Ros-Schuit partition, and the Hirshfeld method. Computations were performed using Multiwfn.

Table S3. The percent contribution of the gold atom of Au_{BCz}^{MAC} to the HOMO and LUMO by different computational methods.

Method	HOMO (%)	LUMO (%)
Mulliken	4.3	9.1
Stout-Politzer	3.5	7.9
Ros-Scuit	4.7	6.9
Hirshfeld	3.4	8.4

Photophysics

Measurements were made in a custom designed glass cuvette equipped with a Teflon valve and side-arm with a small opening. Solutions were initially prepared in ambient conditions, and then they were transferred to the custom cuvettes. Polyethylene tubing was inserted through the side-arm hole with the Schlenk valve open just enough for the tube to pass into the cuvette. The polyethylene tube was lowered into the solution to allow for sparging with N_2. Sparging was performed for ~10 minutes. Finally, the tube was raised past the Schlenk valve but not out of the side-arm under high N_2 flow, and the Schlenk valve was sealed to establish a N_2 atmosphere in the samples. Finally, the tube was removed from the side-arm.

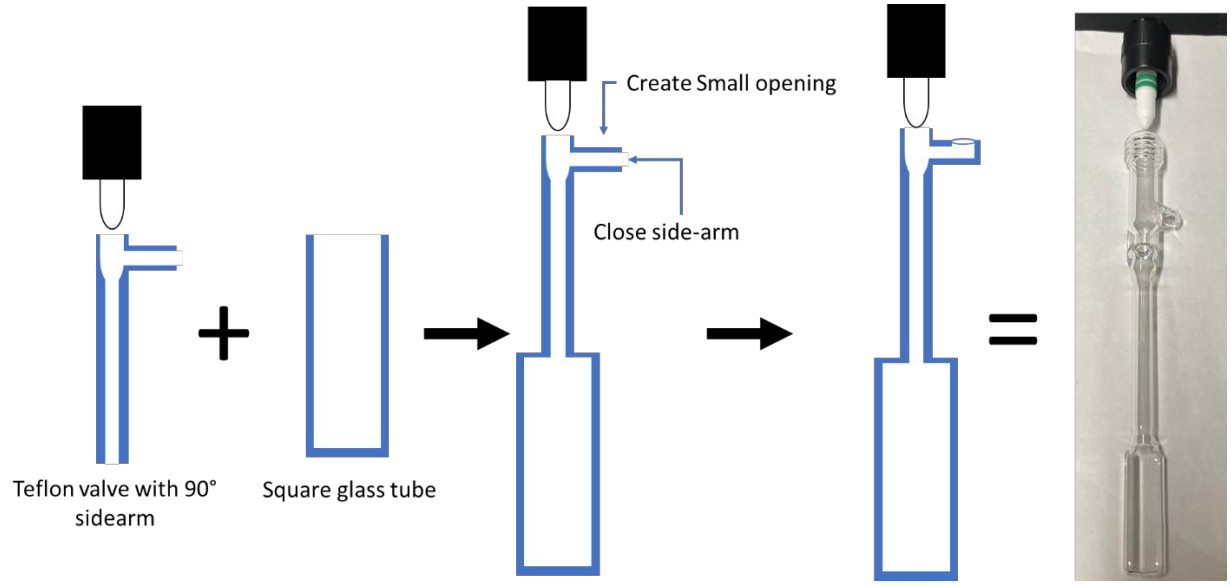

Figure S3. Custom Schlenk cuvettes were made by purchasing a glass joint with a Teflon valve and 90° side-arm. This was fused to a 1cm x 1cm square pyrex tube with the bottom sealed to form the cuvette shape. The side-arm was sealed and a smaller opening was created to make a smaller inlet for the sparging tubing.

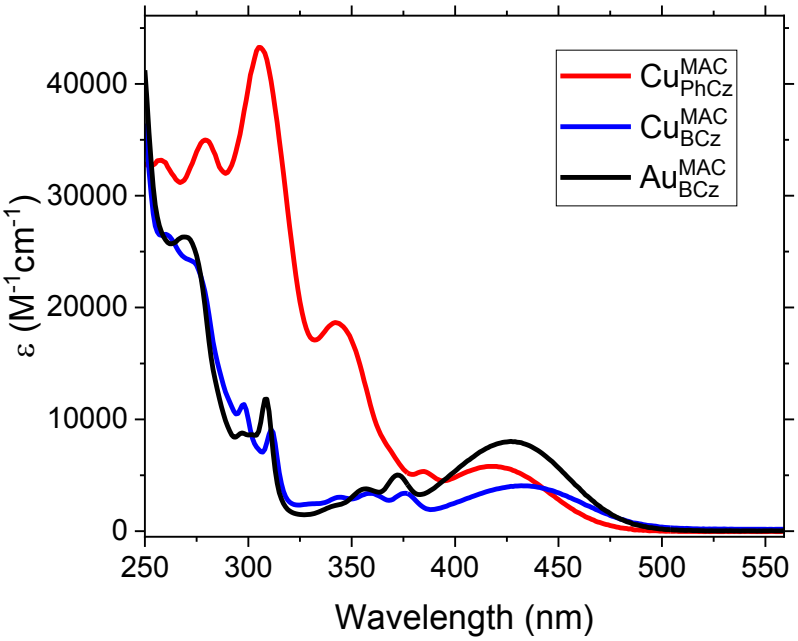

Figure S4. Molar absorptivity spectra in THF for all reported photosensitizers.

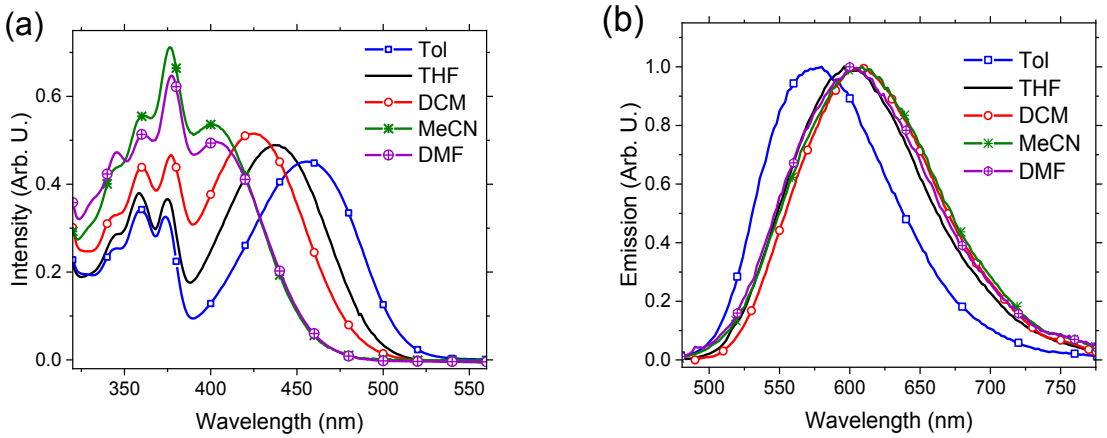

Figure S5. Solvent dependent PL of Cu_{BCz}^{MAC}: (a) absorption, (b) emission.

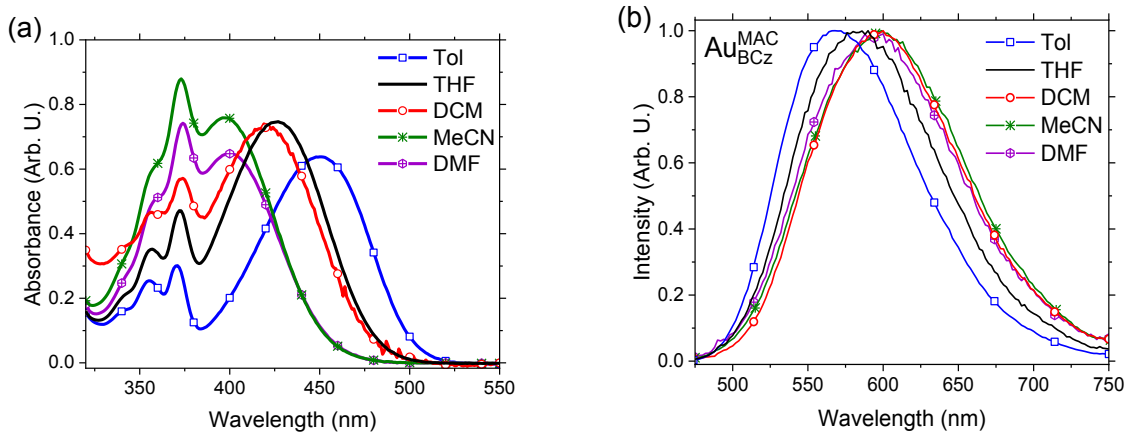

Figure S6. Solvent dependent PL of Au^{MAC}_{BCz}: (a) absorption, (b) emission.

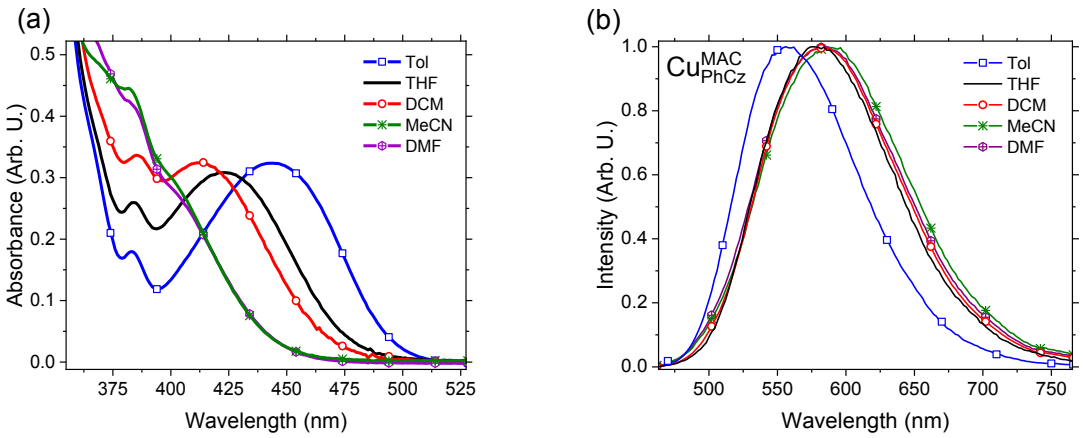

Figure S7. Solvent dependent PL of Cu^{MAC}_{PhCz}: (a) absorption, (b) emission.

Table S4. Photophysical parameters of all reported complexes in toluene, THF, CH_2Cl_2, DMF, and MeCN.

	solvent	λ_{max} abs (nm)	λ_{max} em (nm)	τ (ns)	Φ	k_r ($10^5 s^{-1}$)	k_{nr} ($10^5 s^{-1}$)
Cu_{BCz}^{MAC}	Toluene	455	574	720	0.34	4.7	9.2
	THF	435	603	350	0.17	4.7	24
	CH_2Cl_2	425	608	190	0.10	5.2	47
	DMF	402	607	130	0.04	3.1	74
	MeCN	403	607	120	0.04	3.4	81
Cu_{PhCz}^{MAC}	Toluene	445	556	710	0.70	9.9	4.2
	THF	424	578	460	0.43	9.4	12
	CH_2Cl_2	413	584	330	0.29	8.7	21
	DMF	393*	584	190	0.14	7.6	47
	MeCN	393*	584	190	0.16	8.4	44
Au_{BCz}^{MAC}	Toluene	449	568	450	036	8.0	14
	THF	427	584	250	0.15	6.0	34
	CH_2Cl_2	421	600	130	0.08	6.0	70
	DMF	398	598	75	0.05	6.7	130
	MeCN	400	600	69	0.04	5.8	140

* Values cannot be accurately determined because the ICT absorption band overlaps with the ligand localized transitions at higher energy.

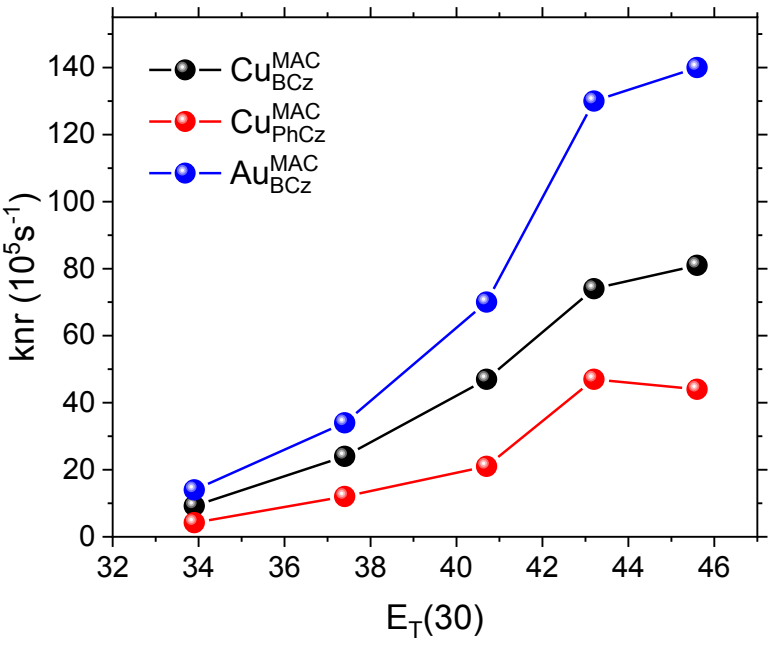

Figure S8. The non-radiative rate vs. solvent $E_T(30)$ of all reported photosensitizers.[1]

Electrochemistry

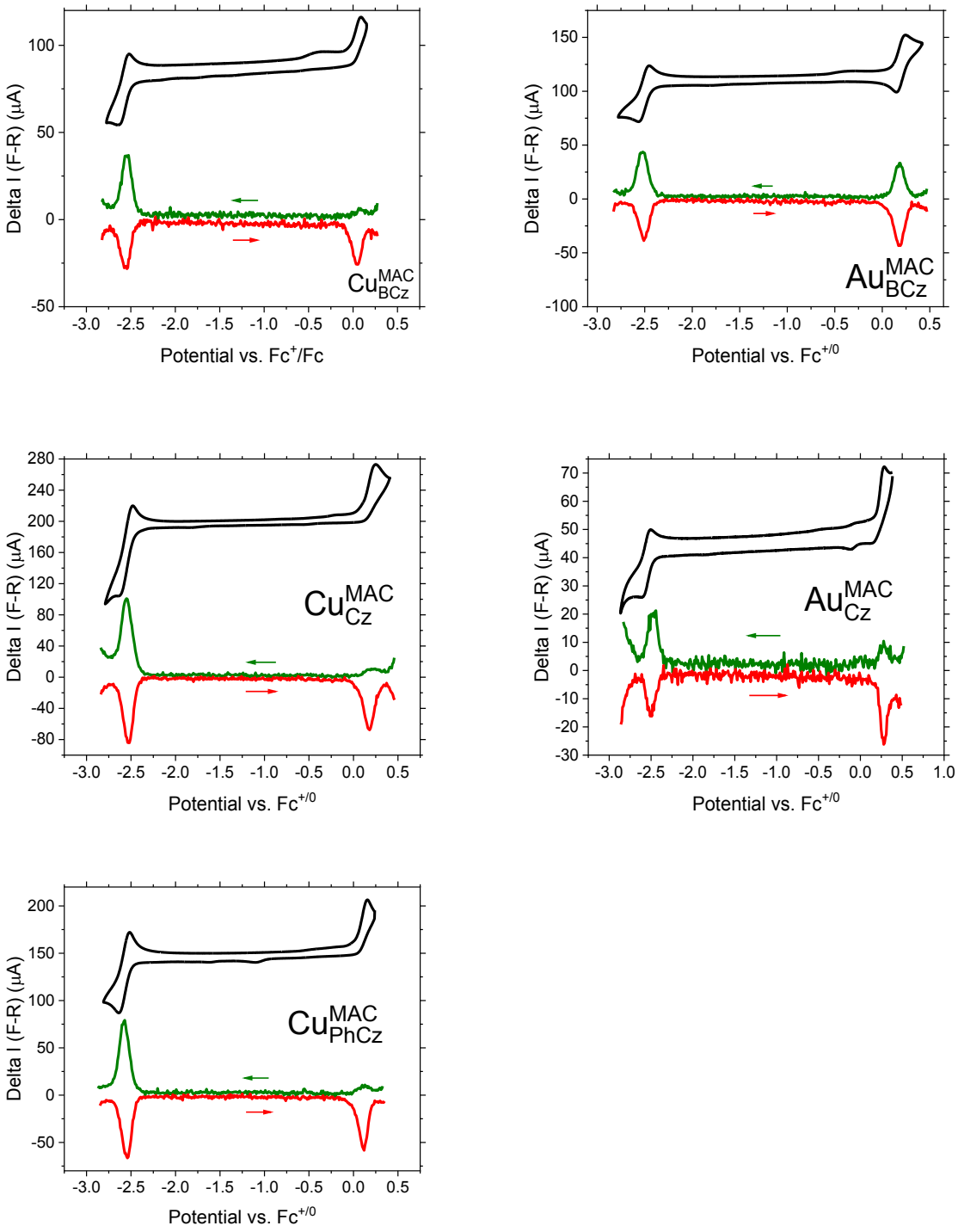

Figure S9. CV and DPV measurements of all reported compounds in DMF vs. $Fc^{+/0}$. The CV scans were vertically shifted to be above the DPV scans during post-processing of the data.

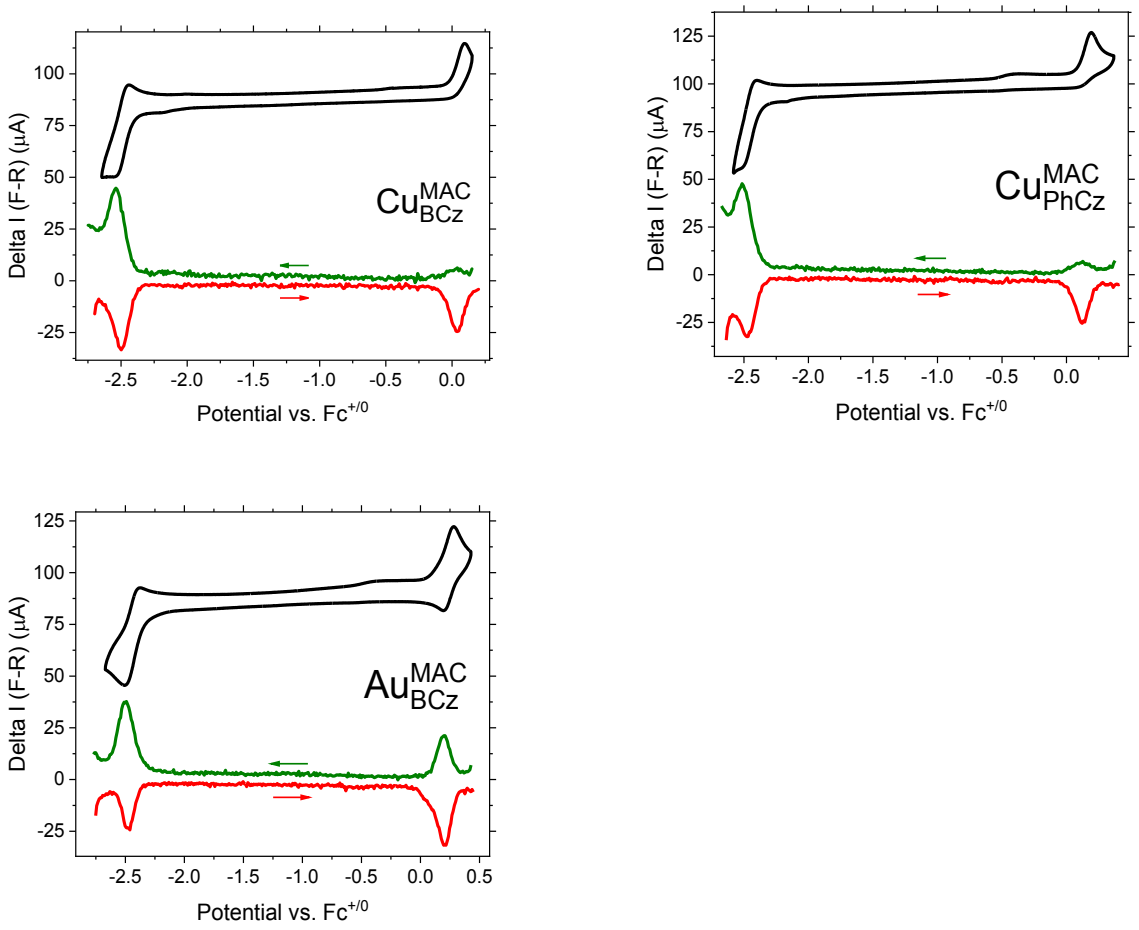

Figure S10. CV and DPV measurements of all reported compounds in MeCN vs. $Fc^{+/0}$. The CV scans were vertically shifted to be above the DPV scans during post-processing of the data.

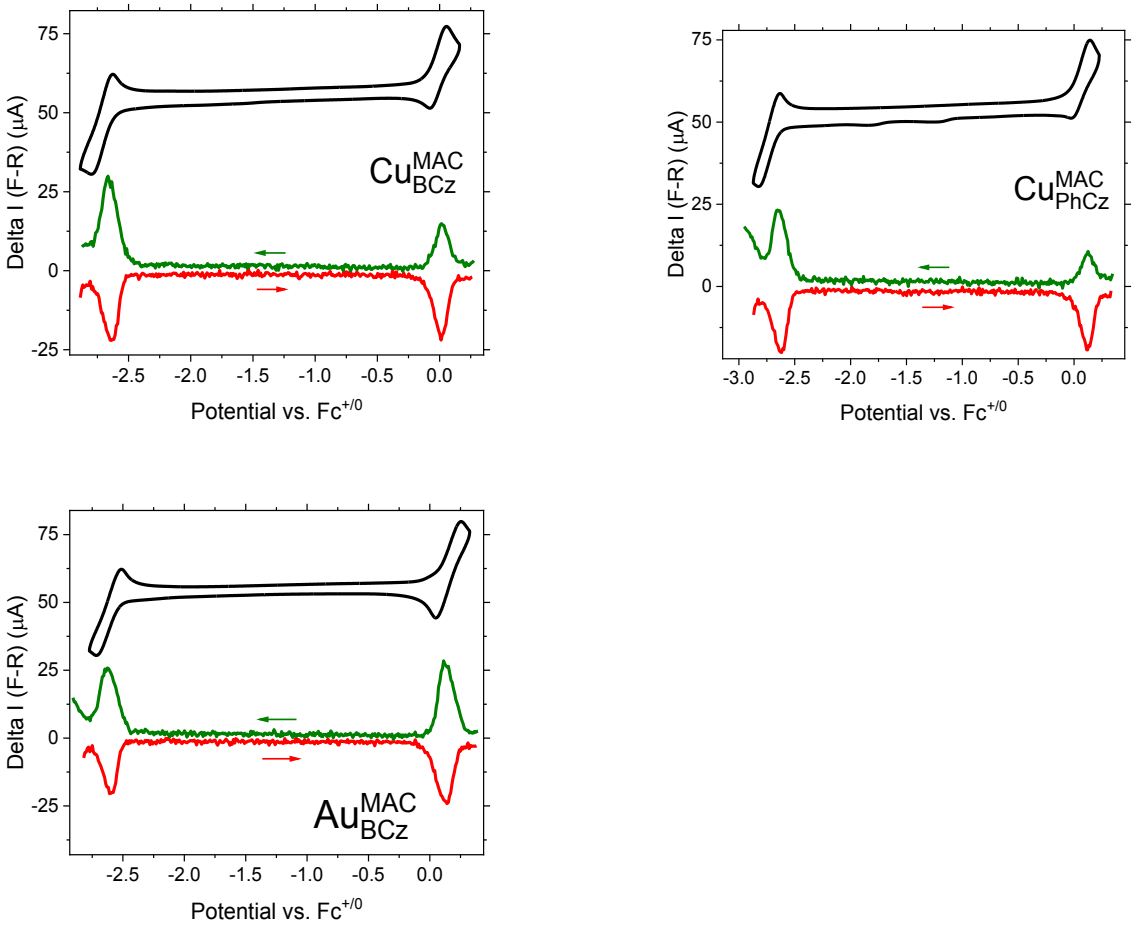

Figure S11. CV and DPV measurements of all reported compounds in THF vs. $Fc^{+/0}$. The CV scans were vertically shifted to be above the DPV scans during post-processing of the data.

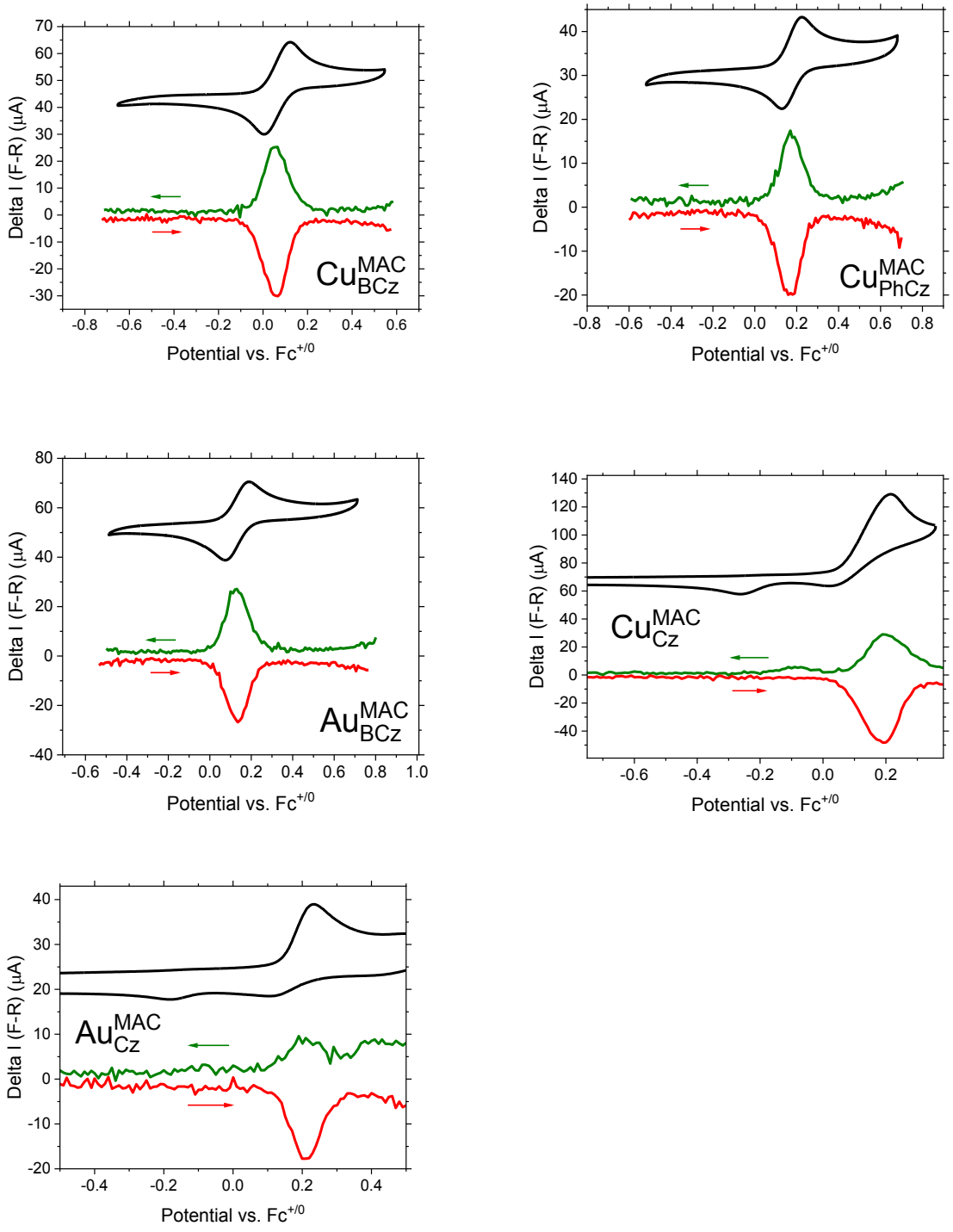

Figure S12. CV measurements of the first oxidation in DCM vs. $Fc^{+/0}$. The reduction event is outside of the solvent window.

Table S5. Electrochemical potentials of cMa complexes in various solvents corresponding to the CV and DPV in Figures S4 – S7.

		$E^{+/0}$ a	$E^{0/-}$ a			$E^{+/0}$ a	$E^{0/-}$ a
CH_2Cl_2	Cu^{MAC}_{BCz}	0.06	b	THF	Cu^{MAC}_{BCz}	0.06	-2.54
	Cu^{MAC}_{PhCz}	0.17	b		Cu^{MAC}_{PhCz}	0.12	-2.62
	Au^{MAC}_{BCz}	0.13	b		Au^{MAC}_{BCz}	0.18	-2.62
	Cu^{MAC}_{Cz}	0.19	b		Cu^{MAC}_{Cz}	0.18	-2.61
	Au^{MAC}_{Cz}	0.22	b		Au^{MAC}_{Cz}	0.28	-2.55
DMF	Cu^{MAC}_{BCz}	0.06	-2.54	MeCN	Cu^{MAC}_{BCz}	0.04	-2.51
	Cu^{MAC}_{PhCz}	0.12	-2.54		Cu^{MAC}_{PhCz}	0.13	-2.52
	Au^{MAC}_{BCz}	0.18	-2.52		Au^{MAC}_{BCz}	0.21	-2.47

[a] Potentials are in Volts vs. Fc+/0 couple, [b] Reductions are outside of the solvent window.

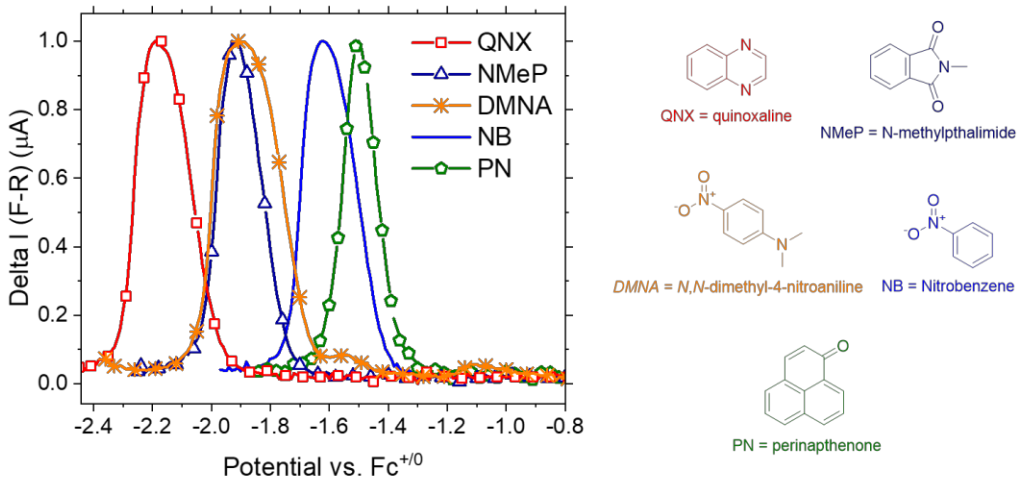

Figure S13. Reductive DPV sweep of electron accepting quenchers that were used to determine $E^{*/+}$ of the cMa complexes in THF (0.1M TBA PF_6).

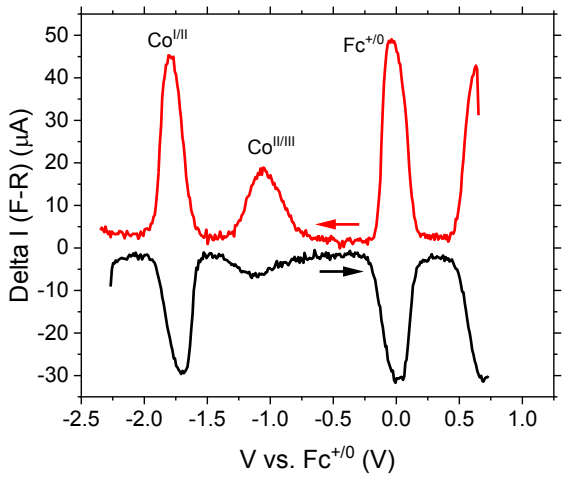

Figure S14. DPV of Co(dmgH)2pyCl in DMF.

Excited State Quenching

Au_{BCz}^{MAC}:

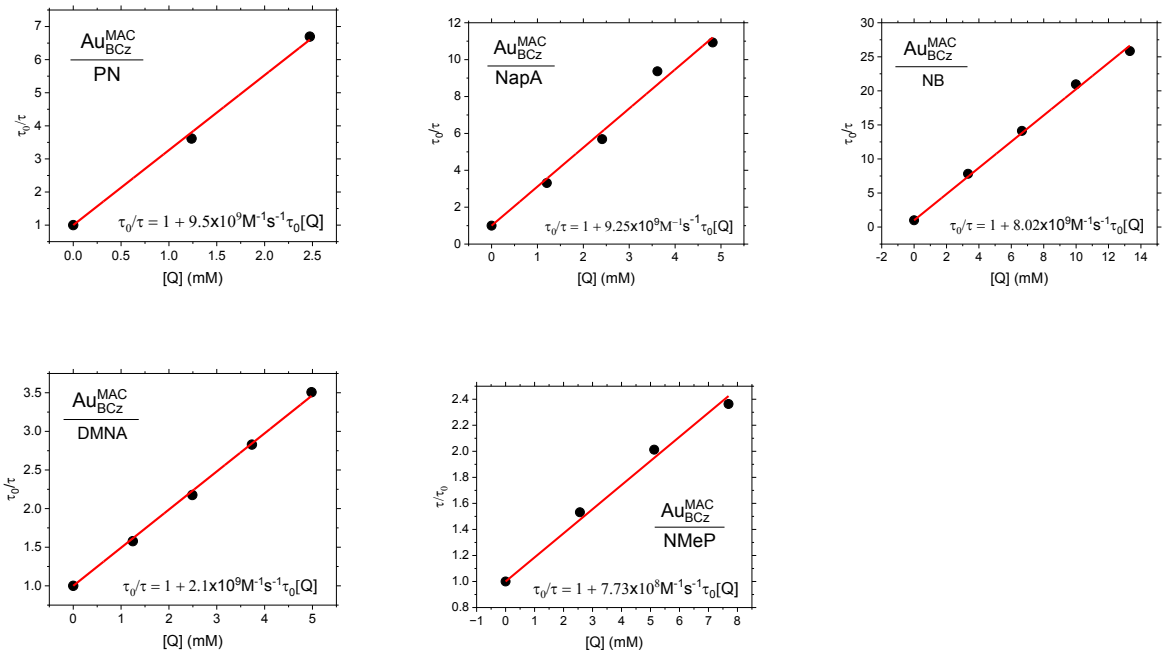

Cu_{BCz}^{MAC}:

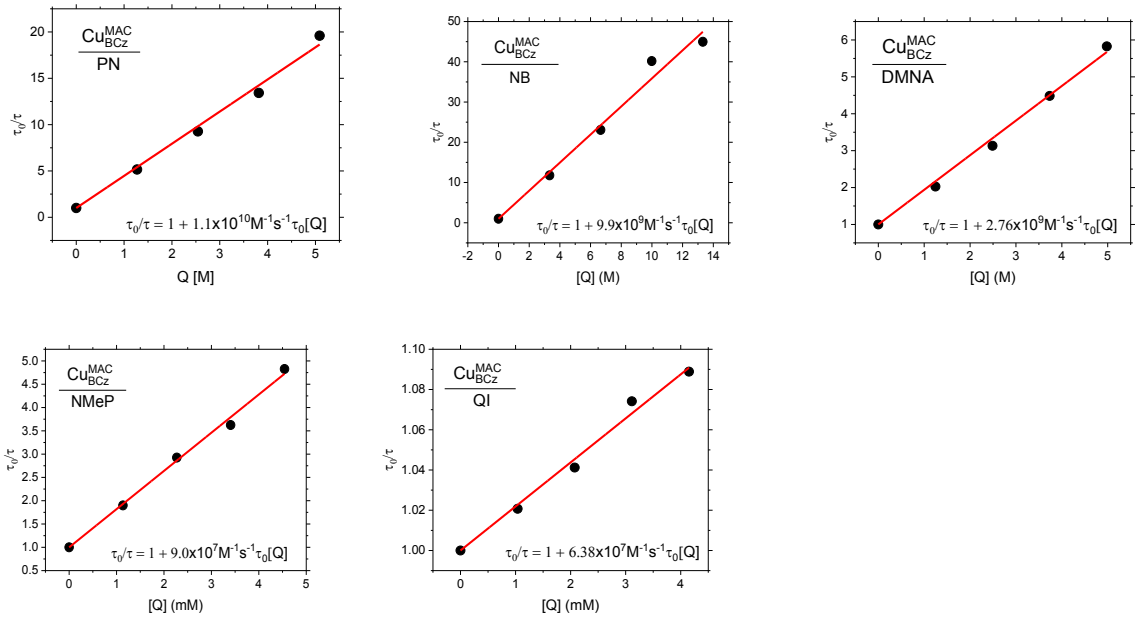

Cu^{MAC}_{PhCz}:

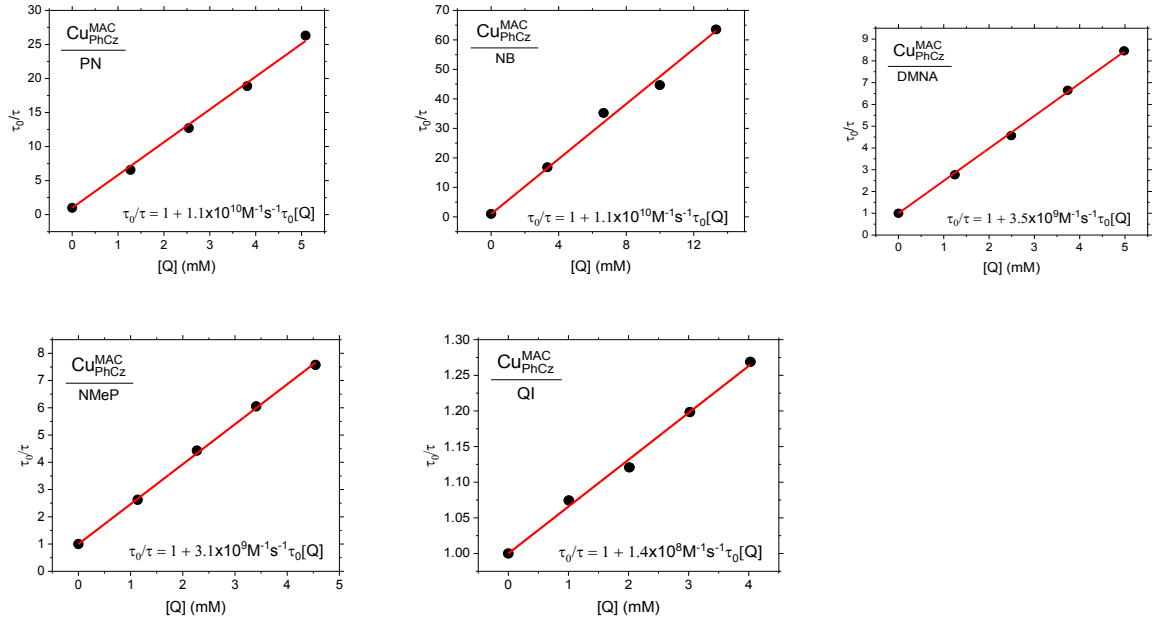

Figure S15. Stern-Volmer plots measured in THF. The corresponding photosensitizer and electron accepting quencher are displayed on the plots.

Cu_{BCz}^{MAC}:

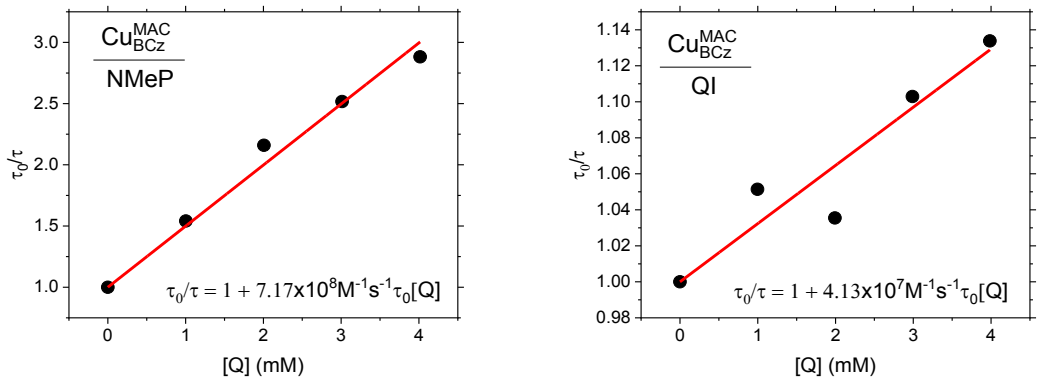

Cu_{PhCz}^{MAC}:

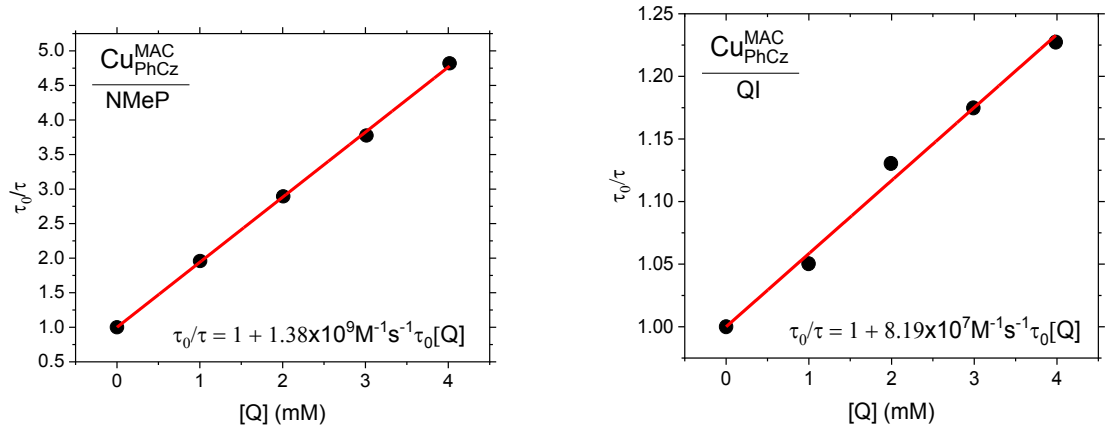

Figure S16. Stern-Volmer plots measured in toluene. The corresponding photosensitizer and electron accepting quencher are displayed on the plots

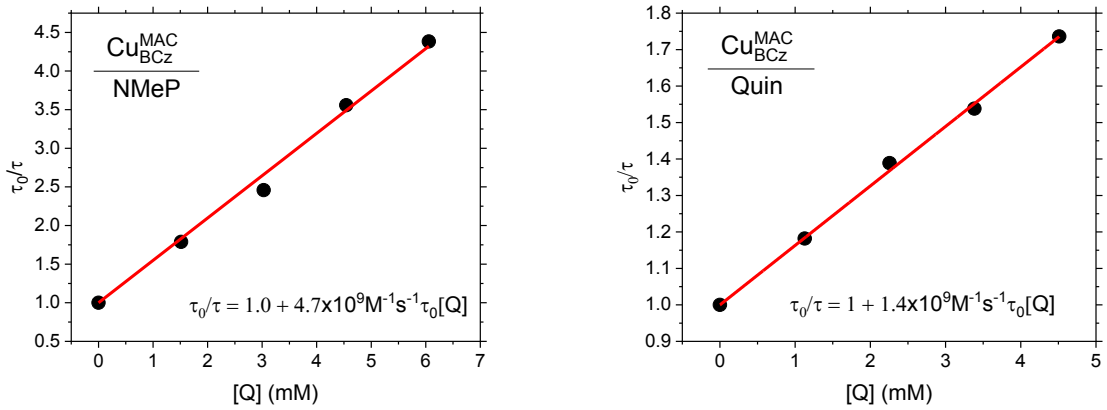

Figure S17. Stern-Volmer plots measured in MeCN. The corresponding photosensitizer and electron accepting quencher are displayed on the plots.

Table S6. Stern-Volmer results of k_q in toluene for all photosensitizers against quinoxaline and n-methyl pthalimide. Au_{BCz}^{MAC} did not yield measurable k_q with quinoxaline or NMeP as an electron accepting quencher.

	V_{red}(V)	$k_q(Cu_{BCz}^{MAC})$ ($M^{-1}s^{-1}10^9$)	$k_q(Cu_{PhCz}^{MAC})$ ($M^{-1}s^{-1}10^9$)
Quin	-2.18	0.04	0.08
NMeP	-1.92	0.71	1.38

Table S7. Stern-Volmer results of k_q in MeCN for all photosensitizers against quinoxaline and n-methyl pthalimide.

	V_{red}(V)	$k_q(Cu_{BCz}^{MAC})$ ($M^{-1}s^{-1}10^9$)
Quin	-2.18	1.4
NMeP	-1.92	4.7

A Rehm-Weller analysis was performed using equations 4-6 in the main text which are re-printed here for reference:

$$\Delta G = \left(E_{PS}^{+/*} - E_{Q}^{0/-}\right) + W_s \quad (4)$$

$$k_q = \frac{k_d}{1 + \left(\frac{k_d}{\Delta V_{12} \times k_{re}}\right)\left(\exp\left(\frac{\Delta G^{\ddagger}}{RT}\right) + \exp\left(\frac{\Delta G}{RT}\right)\right)} \quad (5)$$

$$\Delta G^{\ddagger} = \left[\left(\frac{\Delta G}{2}\right)^2 + (\Delta G_r)^2\right]^{\frac{1}{2}} + \frac{\Delta G}{2} \quad (6)$$

Where $E_{PS}^{+/*}$ is the excited state oxidation potential of the photosensitizer, $E_{Q}^{0/-}$ is the reduction potential of the quenching molecule, W_S is the work term associated with the solvent, R is the ideal gas constant, T is temperature.[2] The free energy term $\Delta G^{\ddagger}$ accounts for the reorganization energy of (PS^*,Q) to (PS^+,Q^-) and the solvent reorganization required for electron transfer ΔG_r. The rate constants k_d, k_{-d}, and k_{re} are from the kinetic scheme shown in Figure 6(c) of the main paper. ΔV_{12} is the equilibrium constant between k_d and k_{-d}.

Fitting k_q vs. $E^{0/-}$ of the quenching molecule provides values of all parameters in equations 4-6 including $E^{+/}*$, W_S, k_d, k_{-d}, k_{re}, and ΔG_r. The reverse process k_{-d} is typically near equivalent to k_d, so ΔV_{12} was set to unity. This yielded the following parameter values with less than 1% error:

Table S8. Parameters from Rehm-Weller fit of k_q vs. $E^{0/-}$ of the quenching molecule.

	$E^{+/*}$ (V vs. $Fc^{+/0}$)	ΔG_r (eV)	W_S (eV)	k_{re} (s^{-1})
$\mathbf{Cu_{BCz}^{MAC}}$	-2.28	0.25	0.1	4.0 x 10^3
$\mathbf{Cu_{PhCz}^{MAC}}$	-2.33	0.25	0.1	4.0 x 10^3
$\mathbf{Au_{BCz}^{MAC}}$	-2.23	0.25	0.1	4.0 x 10^3

The trend in excited state oxidation potential is consistent with the Stern-Volmer quenching experiments. For a given quenching molecule in a given solvent, the measured k_q always increases in the order of $Au_{BCz}^{MAC} < Cu_{BCz}^{MAC} < Cu_{PhCz}^{MAC}$. The Rehm-Weller analysis suggests that this is due to the difference in reductive potency of the excited state $E^{+/}*$ which follows the same trend: $Au_{BCz}^{MAC} < Cu_{BCz}^{MAC} < Cu_{PhCz}^{MAC}$. The solvent reorganization term ΔG_r is within the typical range compared to

other reported systems.[2, 3] The value is consistent for all photosensitizers which can be explained by the similar structural motif of the photosensitizers; they are all two-coordinate carbene-metal-amides. The solvent work term of 0.1 eV is reasonable and consistent between all photosensitizers which is to be expected, because W_S is an intrinsic property of the solvent.[4] Lastly, k_{re} is consistent between all photosensitizers and suggests the charge separated pair (PS^+,Q^-) recombines to the ground state (PS,Q) with a time constant of 250μs.

Photocatalysis

Figure S18. Experimental Setup for photocatalysis**.**

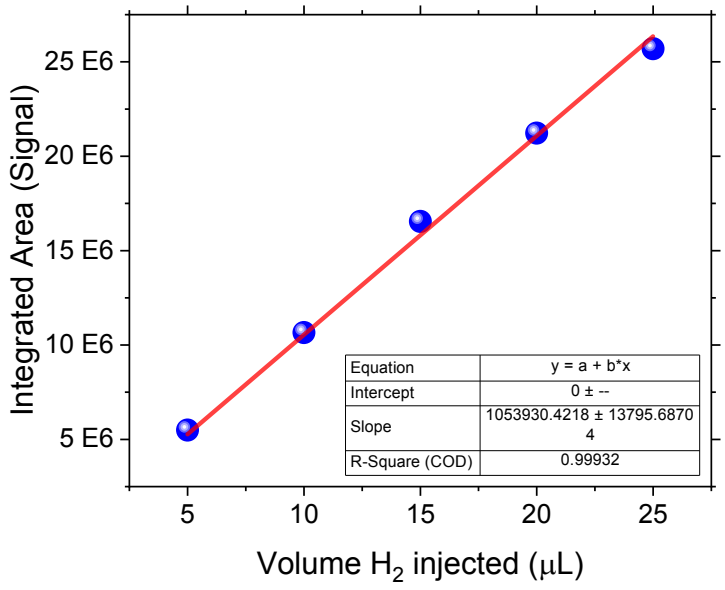

Figure S19. GC H_2 calibration curve**.**

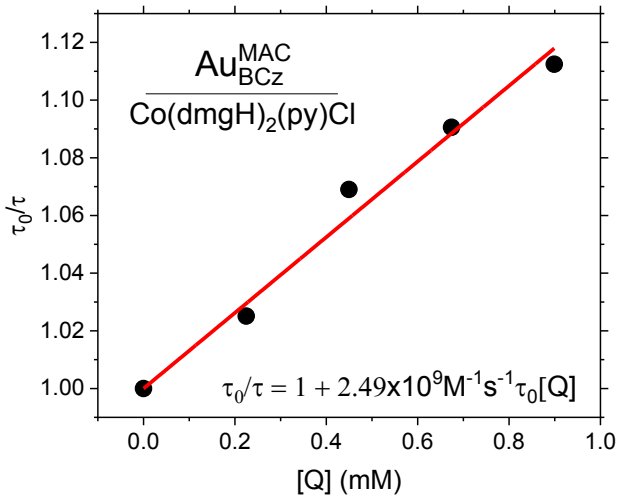

Figure S20. Stern-Volmer study of Au^{MAC}_{BCz} quenched by $Co(dmgH)_2pyCl$ in THF. The k_q is near diffusion limited as predicted by the Rehm-Weller analysis.

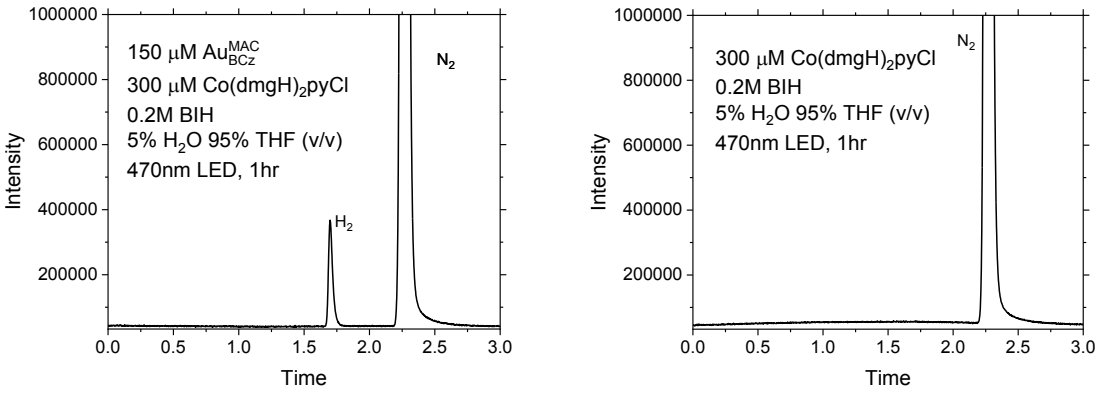

Figure S21. Irradiation of the sample with (left) and without (right) the photosensitizer as a control experiment. This proves that the photosensitizer is necessary to generate H_2.

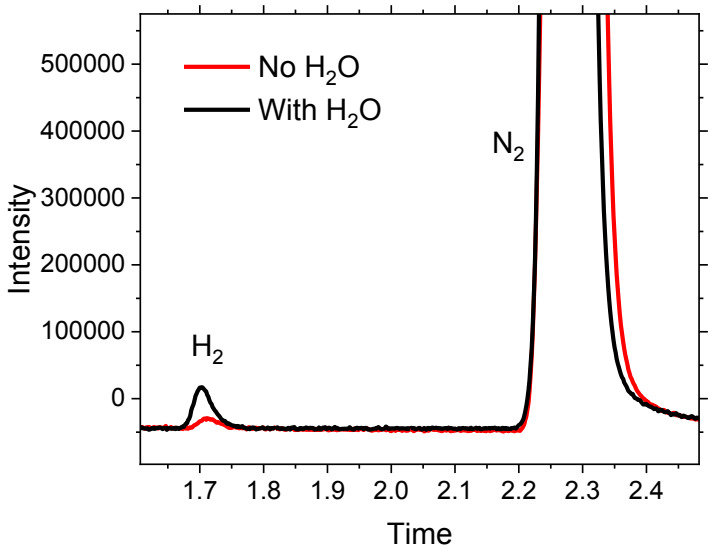

Figure S22. Control experiment of photo driven HER with and without water after one hour of irradiation in a 355 nm photoreactor chamber.

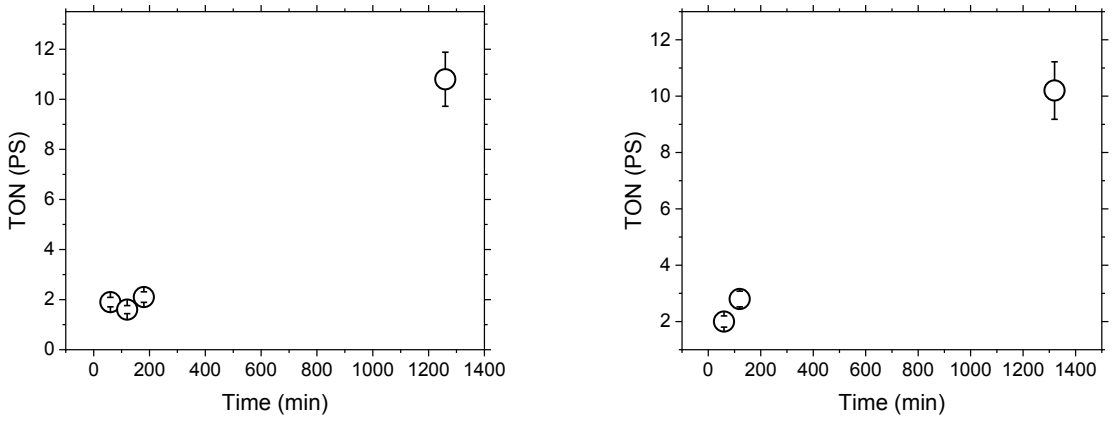

Figure S23. Photocatalysis without Co(dmgH)$_2$pyCl. Samples were prepared with 160 μM Au^{MAC}_{BCz} (left), and 63 μM Cu^{MAC}_{PhCz} (right) in wet THF (5% water by vol), 200 mM BIH, and irradiated with a 470 nm LED.

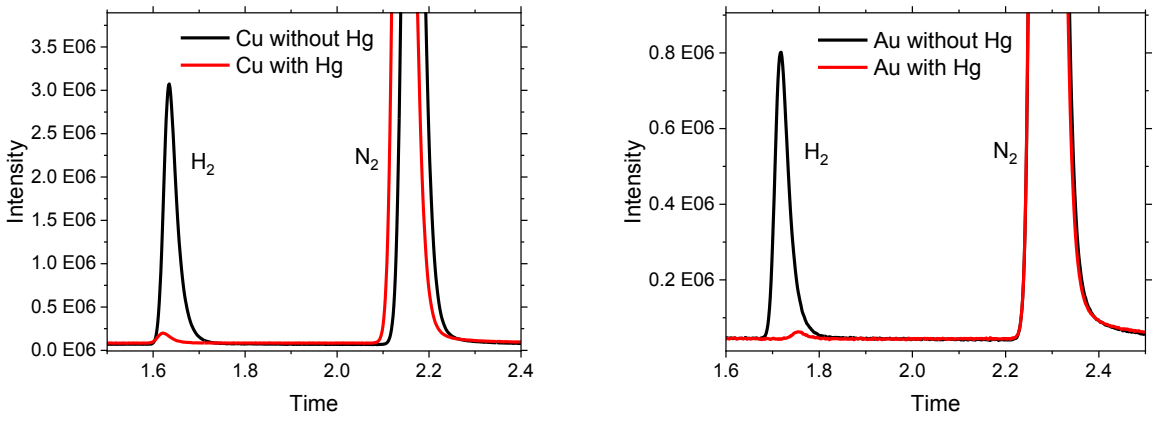

Figure S24. Mercury poisoning tests after ~23 hrs of irradiation without $Co(dmgH)_2pyCl$ for Cu^{MAC}_{PhCz} (left), and Au^{MAC}_{BCz} (right). The concentrations of the photosensitizer these experiments were ~ 300 μM for the copper experiments, and ~150 μM for the gold experiments.

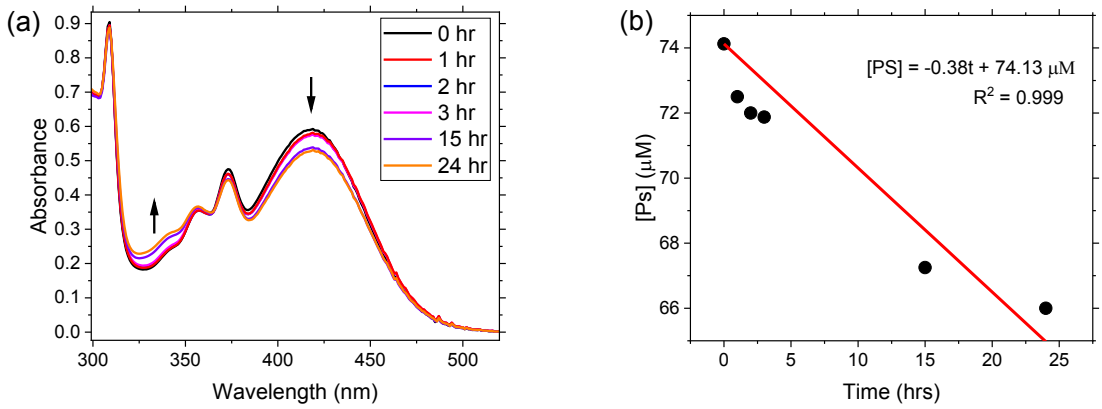

Figure S25. Photostability of Au^{MAC}_{BCz} in air free THF/water (5% v/v) irradiated with a 470nm LED at ~486 mW intensity. The absorption spectrum (a) and the concentration of Au^{MAC}_{BCz} calculated using Beer's law (b).

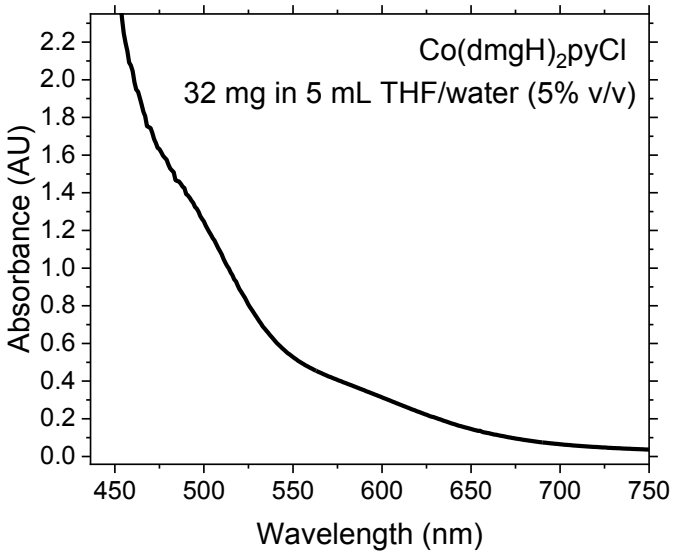

Figure S26. Absorption spectrum of a saturated $Co(dmgH)_2pyCl$ solution in THF/water (5% v/v).

NMR

^{1}H and ^{13}C NMR Spectra

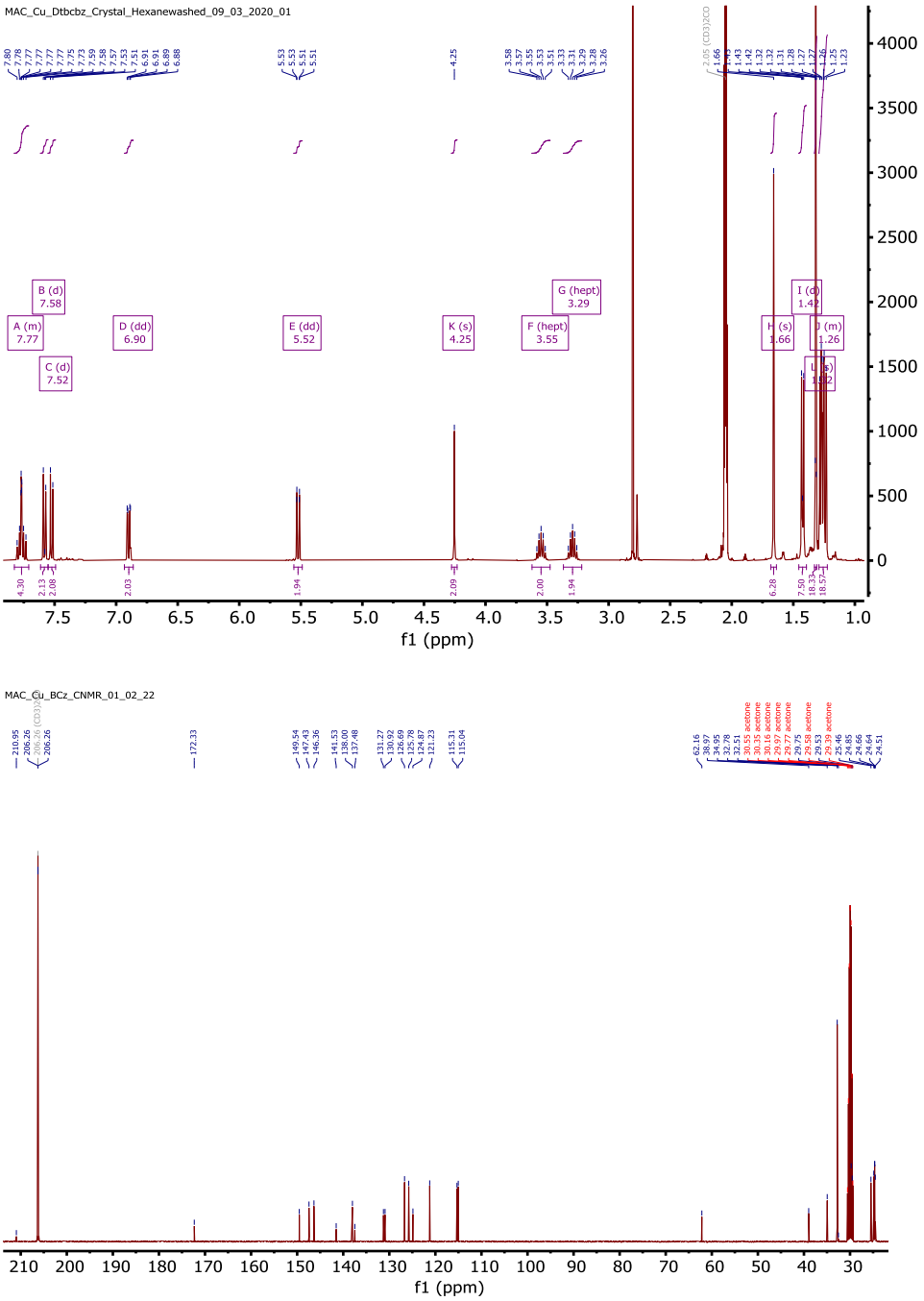

Figure S27. ^{1}H and ^{13}C NMR of Cu_{BCz}^{MAC} in acetone-d6. The peaks at 2.05 ppm and 2.8 ppm in the ^{1}H NMR correspond to acetone and water respectively.

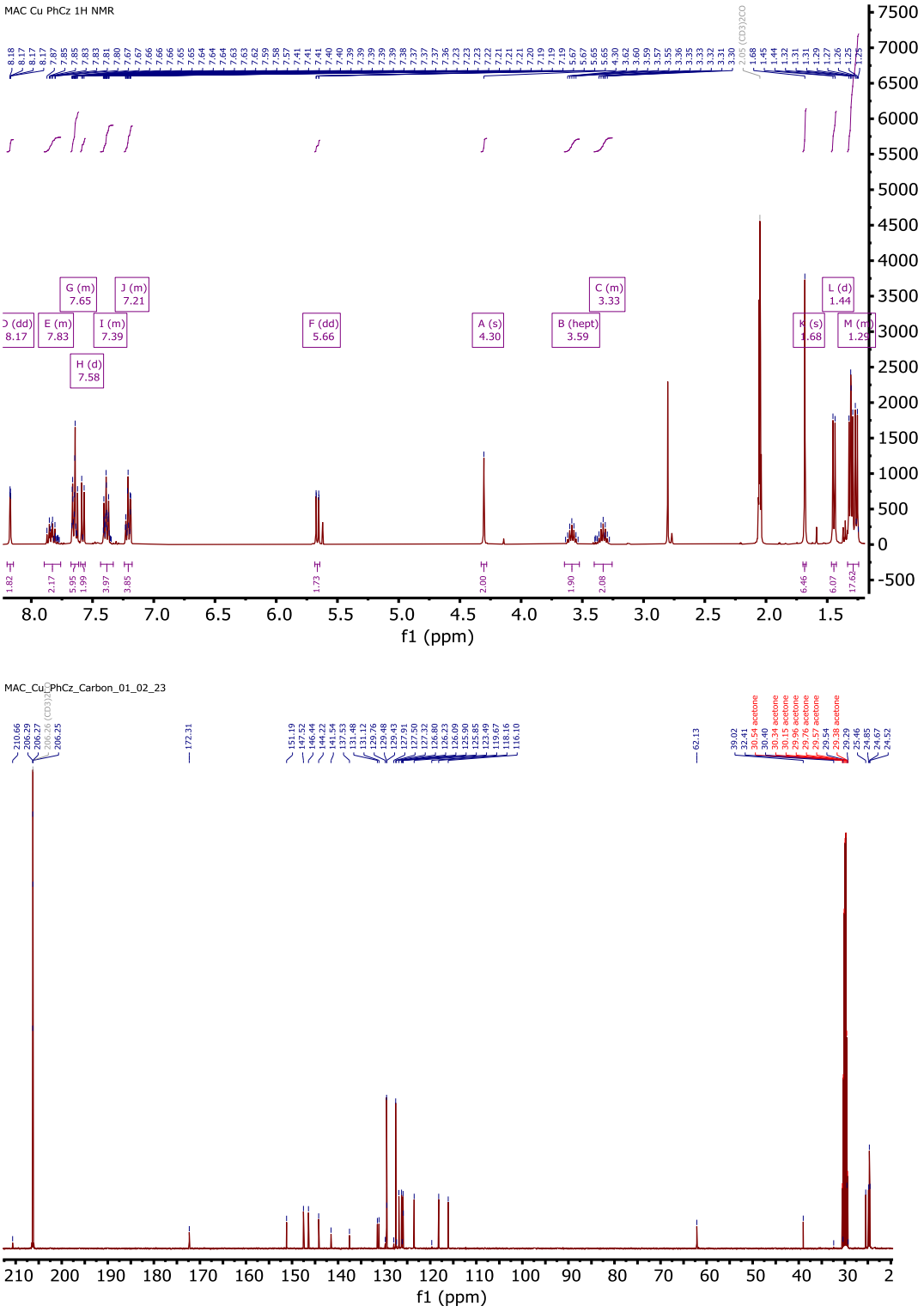

Figure S28. ^{1}H and ^{13}C NMR of Cu^{MAC}_{PhCz} in acetone-d6. The peaks at 5.2 ppm, 2.8 ppm, and 2.05 ppm in the ^{1}H NMR correspond to DCM, water, and acetone-d6 respectively.

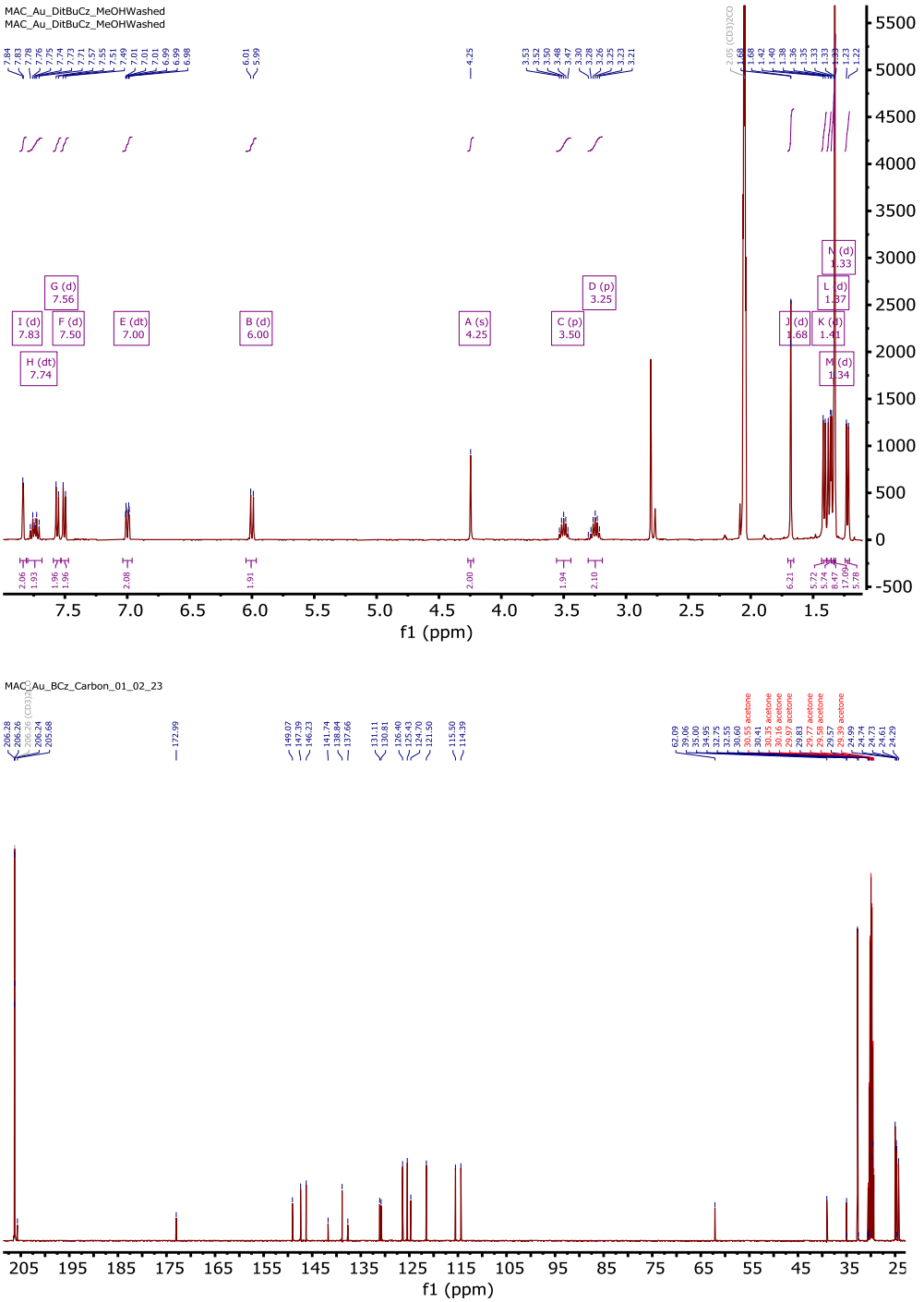

Figure S29. ^{1}H and ^{13}C NMR of Au_{BCz}^{MAC} in acetone-d6. The peaks at 2.05 ppm and 2.8 ppm in the ^{1}H NMR correspond to acetone and water respectively.

1. Weinkauf, J. R.; Cooper, S. W.; Schweiger, A.; Wamser, C. C., Substituent and Solvent Effects on the Hyperporphyrin Spectra of Diprotonated Tetraphenylporphyrins. *The Journal of Physical Chemistry A* **2003,** *107* (18), 3486-3496, DOI: 10.1021/jp022046f

2. Rehm, D.; Weller, A., Kinetics of Fluorescence Quenching by Electron and H-Atom Transfer. *Israel Journal of Chemistry* **1970,** *8* (2), 259-271, DOI: 10.1002/ijch.197000029

3. Bevernaegie, R.; Wehlin, S. A. M.; Piechota, E. J.; Abraham, M.; Philouze, C.; Meyer, G. J.; Elias, B.; Troian-Gautier, L., Improved Visible Light Absorption of Potent Iridium(Iii) Photo-Oxidants for Excited-State Electron Transfer Chemistry. *Journal of the American Chemical Society* **2020,** *142* (6), 2732-2737, DOI: 10.1021/jacs.9b12108

4. Ma, B.; Djurovich, P.; Thompson, M., Excimer and Electron Transfer Quenching Studies of a Cyclometalated Platinum Complex. *Coordination Chemistry Reviews* **2005,** *249*, 1501-1510, DOI: 10.1016/j.ccr.2005.02.004